TIMOTHY A.V. TEATRO

Dynamical Effects in Crystalline Solid State Systems

*Theory of Temperature Dependent Optical Response
of Bulk GaAs and Vibrational Modification of
C(111) 2×1 Surface in Comparison to Experiment*

UOIT
CHALLENGE INNOVATE CONNECT

A THESIS SUBMITTED IN PARTIAL FULFILLMENT OF THE
REQUIREMENTS FOR THE DEGREE OF
MASTER OF SCIENCE
AT
THE UNIVERSITY OF ONTARIO INSTITUTE OF TECHNOLOGY
FACULTY OF SCIENCE
APRIL, 2009

UNIVERSITY OF ONTARIO INSTITUTE OF TECHNOLOGY

Author: **Timothy A.V. Teatro**

Title: **Dynamical Effects in Crystalline Solid State Systems**

Faculty: **Faculty of Science**

Degree: **M.Sc**   Submission Date: **July 4, 2009**

Permission is herewith granted to University of Ontario Institute of Technology to circulate and to have copied for non-commercial purposes, at its discretion, the above title upon the request of individuals or institutions.

_____
Signature of Author

Abstract

This thesis presents a new theoretical formalism which incorporates dynamical effects in atomistic electronic structure and related calculations.

This research, fundamental by nature, brings about a deeper understanding of the dynamical processes in a range of materials. This establishes technologically important correlation with experimentally measured macroscopic properties and materials characterization. This method—the first of its kind—is a natural and long overdue extension of customary adiabatically separated time-independent electronic structure methods. It accounts explicitly for atomic motion due to thermal and zero-point vibration. The approach developed requires no direct treatment of time dependence in the quantum mechanical calculations, making the method widely applicable utilizing currently available electronic structure and *ab-initio* molecular dynamics software.

The formalism is extensively applied and demonstrated for the linear optical response of bulk gallium arsenide and electronic structure of the $C(111) \, 2 \times 1$ surface. Both cases are complimented by comparison of key observables to experimental data which may be used to judge the quality of the results. The results are found to be in good agreement with experimental data, with most exceptions being readily explainable and well understood.

Keywords: dynamical effects, thermally perturbed band structure and optical response, dielectric properties, gallium arsenide, semiconductor surfaces, zero-point vibrations, $C(111) \, 2 \times 1$ reconstruction.

To my Mom, Dad and Grandma

&

my wife to be, Lindsay.

Words could never express my love and gratitude.
From the depths of my heart,
    thank you.

                                    Tim.

Acknowledgements

I GRATEFULLY acknowledge the caring guidance of my supervisor, Prof. Anatoli Shkrebtii, from whom I have learned for many years. He has not only taught me the science which I love, he has shown me how to be a scientist. This is a debt which I could never repay. I'd like similarly to thank Prof. Franco Gaspari who has also trustfully guided me over the years.

I also acknowledge, most gratefully, the contributions to this research made by Prof. Chkrebtii's post-doctoral fellows, Dr. Zahraa Ibrahim and Dr. Ihor Kupchak, who have been been wonderfully helpful in several key areas. Zahraa and I have worked collaboratively on our group's GaAs research, and I have benefited greatly from her insightful advice.

A special thanks goes out to the Condensed Matter Theory Group at the University of Rome Tor Vergata, for their collaborative efforts in our $C(111)\, 2 \times 1$ surface research. Thank you to Dr. Olivia Pulci and Dr. Margherita Marsili for many insightful e-mail exchanges with our group.

My colleagues and I sadly but fondly bid farewell to Martin J.G. Lee (1942–2009), and acknowledge his great contributions to the optical calculations early in the GaAs research. His wisdom will echo through the many lives he has touched.

Finally, I'd like to thank my mom and dad, my grandmother and my wonderful fiancée, Lindsay. They have helped me in every aspect of my life so that I could spend many hours in 'my hole' working on my research and this thesis. I can't overstate their contributions to my work and my life. This thesis is dedicated to them with boundless love and gratitude.

Oshawa, Ontario   Timothy A.V. Teatro
June 11, 2009

CONTENTS

LIST OF TABLES

LIST OF FIGURES

List of Acronyms

AIMD	*ab-initio* molecular dynamics		**HOMO**	highest occupied molecular orbital
APW	augmented plane-wave		**IBZ**	irreducible Brillouin zone
APW+lo	augmented plane-wave with local orbitals		**KS**	Kohn-Sham
BFGS	Broyden-Fletcher-Goldfarb-Shanno		**LAPW**	linearised augmented-plane-wave
BO	Born-Oppenheimer		**LDA**	local density approximation
BOMD	Born-Oppenheimer molecular dynamics		**lo**	local orbitals
BZ	Brillouin zone		**LUMO**	lowest unoccupied molecular orbital
CP	Car-Parrinello		**MD**	molecular dynamics
CPMD	Car-Parrinello molecular dynamics		**MP**	Monkhorst-Pack
DB	dangling bonds		**MSD**	mean-square displacement
DFT	density functional theory		**MT**	muffin tin
DOS	density of states		**PBE**	Perdew, Burke and Ernzerhof
DFT-LDA	density functional theory under the local density approximation		**PP**	pseudopotential
FCC	face centred cubic		**PWP**	plane-wave pseudopotential
FFT	fast Fourier transform		**RPA**	random phase approximation
FP-LAPW	full-potential linearised augmented-plane-wave		**SBZ**	surface Brillouin zone
			SCF	self consistent field
GGA	generalized gradient approximation		**SO**	spin-orbit
GS	ground state		**TF**	Thomas-Fermi
HF	Hartree-Fock		**VAC**	velocity autocorrelation
			VDOS	vibrational density of states
HK	Hohenberg-Kohn		**XC**	exchange-correlation

Preface

This thesis is submitted for the degree of Master of Science at the University of Ontario Institute of Technology in the field of Materials Science. It contains an account of a small portion of research carried out between September 2008 and June 2009 at the Faculty of Science under the supervision of Prof. Dr. A. I. Chkrebtii. While some parts of this research have been a collaborative effort, all calculations and other work presented herein were performed independently, unless otherwise indicated. No part of this thesis has been or is currently being submitted for any degree or diploma at this, or any other, University.

Timothy A.V. Teatro

LIST OF PUBLICATIONS

Parts of this work have been published, or are in preparation for publication in the following:

- T. Teatro, A. I. Shkrebtii, and I. M. Kupchak. C(111)2x1 revisited: quantum zero point motion contribution to atomic structure, dynamics and electronic bands. *In preparation for Surface Science*.

- Z.A. Ibrahim, A.I. Shkrebtii, T. Teatro, and M.J.G. Lee. First-principles temperature dependence of the electronic structure and optical response of bulk GaAs based on molecular dynamics simulations. *In preparation for Phys. Rev. B*.

- A.I. Shkrebtii, Z. Ibrahim, M.J.G. Lee, T. Teatro, W. Richter, M. Drago, and T. Trepk. Lattice dynamics and the optical properties of semiconductors: theory of the temperature dependent dielectric functions of GaAs and Si and comparison with experiment. In *Proceedings of International Conference on the Physics of Semiconductors - ICPS 2008*, Rio de Janeiro, Brazil, 2008.

- Z. A. Ibrahim, A. I. Shkrebtii, M. J. G. Lee, K. Vynck, T. Teatro, W. Richter, T. Trepk, and T. Zettler. Temperature dependence of the optical response: Application to bulk GaAs using first-principles molecular dynamics simulations. *Physical Review B (Condensed Matter and Materials Physics)*, 77(12):125218, 2008.

LIST OF PRESENTATIONS

Parts of this work have been or is to be exhibited in the following conference presentations, seminars and colloquia:

- Trieste, Italy, Oct. 2009. Future presentation at SMR 2054: Structure and Dynamics of Hydrogen-Bonded Systems, The Abdus Salam International Centre for Theoretical Physics (ICTP).

- F. Gaspari, A. Shkrebtii, and T. Teatro. Computational aspects of the modelling of vibrational properties of gases, liquids and solids. Rhodes (Crete, Greece), Sept.–Oct. 2009. to be presented by F. Gaspari.

- Weimar, Germany, July 2009. Two presentations at 12th International Conference on Formation of Semiconductor Interfaces (ICFSI-12).

- Z. Ibrahim, M. J. G. Lee, W. Richter, I. Kupchak, M. Drago, T. Trepk, T. Teatro, and F. Gaspari. Role of lattice dynamics in temperature dependent optical response, vibrational spectra, and chemical bonding in semiconductor materials: theory versus experiment. Paris, France, 2008. Invited seminar at Institut des NanoSciences de Paris (INSP) at UPMC (Univ. Pierre & Marie Curie).

- Z. Ibrahim, M. J. G. Lee, W. Richter, I. Kupchak, M. Drago, T. Trepk, T. Teatro, and F. Gaspari. Temperature dependent optical response in semiconductors: numerical formalism v.s. experiment for GaAs and Si. Excitonic effects wanted! Paris, France, 2008. Invited seminar at Laboratoire des Solides Irradiés, Ecole Polytechnique, CEA, CNRS.

- Z. Ibrahim, M. J. G. Lee, W. Richter, I. Kupchak, M. Drago. , T. Trepk, T. Teatro, and F. Gaspari. First-principles modeling of structure, vibrations, bond dynamics, electronic and optical properties in hydrogenated amorphous silicon: theory versus experiment. Braga, Portugal, 2008. Invited seminar at Centro de Fisica, Universidade do Minho.

- A.I. Shkrebtii, Z. Ibrahim, M.J.G. Lee, T. Teatro, W. Richter, M. Drago, and T. Trepk. Lattice dynamics and the optical properties of semiconductors: theory of the temperature dependent dielectric functions of GaAs and Si and comparison with experiment. Rio de Janeiro, Brazil, 2008. Jul 27–Aug 1.

- A. Shkrebtii, M. Lee, T. Teatro, W. Richter, T. Zettler, and T. Trepk. Linear optical response of bulk GaAs from finite-temperature lattice dynamics. Los Angeles California USA, 2005. American Physical Society March Meeting.

INTRODUCTION

THE field of solid state physics observes an interesting mutualism with computing technology. As the field of solid state physics evolves, it affords us the knowledge to build better and more powerful computers, which in turn allows scientists to reveal more about the physics of solid state. Many of the problems faced by solid state physicists over the past several decades found resolution only when computers had become powerful enough to simulate the appropriate relationships. This is no less the case now than it has been in the past. Our problems however have scaled incredibly as our picture of the universe becomes more precise. With the expanding capabilities of computers, new methods must be created, or old ones updated. Restrictive assumptions and simplifying ansätze can be removed, exposing natural truths which were obscured for the sake of computational simplicity.

We present here, an approach which extends traditional implementations of density functional theory—a popular approach to ground state atomistic modelling—to explicitly account for the interaction of electrons with quantized vibrations of the lattice (phonons). Such interactions are important for truly predictive modelling of real systems.

Even as experimental samples are cooled near the absolute-zero temperature limit, their nuclei vibrate intrinsically to satisfy the quantum mechanical uncertainty principle. The electrons around the nuclei are constantly reconfigured in response to this motion.

In nearly all cases, when experiments are modelled, such effects are neglected because they add a considerable layer of complexity to the problem. Through the use of standard methods of *ab-initio* molecular dynamics, we model the vibrations of crystal lattices, and use these data to understand the effects of the vibrations on the electronic structure of the system.

In the first chapter, the reader is presented with a brief primmer on first principles electronic structure methods and *ab-initio* molecular dynamics, with emphasis on density functional theory. Several of the most common approaches to various aspects of density functional theory are described, including the pseudopotential approximation, local density

and generalized gradient approaches to exchange and correlation as well as plane-wave and augmented plane-wave with local orbitals basis sets. The two main approaches to *ab-initio* molecular dynamics, those of Car–Parrinello and Born–Oppenheimer, are also described.

In the second chapter, we present results of simulations modelling the temperature dependence of the linear optical response of gallium arsenide—a key material in the worlds of alternative energy and electronics. The optical response of a crystal is signature of its electronic structure and is very sensitive to the atomic structure of the lattice. The effects of vibrations and temperature are readily observable from this quantity, making it an excellent gauge for the accuracy of our model. The results of our calculations are complimented by a direct and thorough comparison to the experimentally obtained data of our collaborators, which verifies the validity of the approach.

Finally, in the third chapter, we look directly at the electronic structure of the $C(111) 2 \times 1$ surface—a topic of great controversy and mystery for more than two decades. While similar surfaces for other group–IV elements are well understood, the $C(111) 2 \times 1$ surface remains elusive. Recent state-of-the-art calculations by our collaborators in Rome have taken a major leap in this area with very advanced electronic structure calculations. These calculations however are hindered by a fundamental issue which we show can be resolved when electron–phonon effects are considered within our method. We further this with an in-depth study of vibrational properties of the surface where modes of vibration are linked directly to a specific physical mechanism governing key properties of the electronic structure.

Through these examples, a deeper understanding of the dynamical processes which govern the interaction between electrons and phonons is gained. Along the way, we explain the real world physics behind the mathematical labyrinth which leads to our results. These results, and the knowledge that they represent, are fundamental and relevant to the field of solid state physics.

1

FIRST PRINCIPLES THEORY OF ELECTRONIC STRUCTURE AND *Ab-Initio* MOLECULAR DYNAMICS

MUCH of the work presented here is based on calculations of the structure of an inhomogeneous gas of electrons surrounding a lattice of nuclei. Because the behaviour of electrons in such a system is inherently quantum, many of the physical properties of solid state systems depend on a strict and precise treatment of quantum physics. A logical means to treat the problem is through the solution of Schrödinger's equation for the many-body system to obtain the many-body wave-function, Ψ.

It was in 1926 that Erwin Schrödinger first defined the eigenvalue problem of wave mechanics [1]. Built upon Louis de Broglie's extraordinary realization that material particles were not point-masses, but wave-systems ("ondes de phase" or *phase-waves*), Schrödinger's quantized eigenvalue problem paved the way for scientists to model and understand the nature of the microscopic world. Schrödinger's wave equation, $i\hbar\dot{\Psi} = H\Psi$, defines the mechanics of the many-body wave-function as it is acted upon by the system Hamiltonian operator H associated with the total energy. The time separation of Schrödinger's equation leads to a discrete set of eigenvalues, $\{E_i\}$, corresponding to the stationary wave-functions $\{\psi_i\}$ which define the properties of the system.

Like its Newtonian analogue, Schrödinger's quantum wave mechanics is analytically intractable for three or more interacting bodies. Computational models can be used to solve the problem for N interacting bodies; but practical electronic structure calculations for solids or molecules require numerical analysis in which many simplifying assumptions are made. Without these assumptions, the problem quickly grows far beyond the capabilities of

3

state-of-the-art computing hardware.

Less than two years after Schrödinger's landmark paper, D.A. Hartree proposed the *self consistent field (SCF)* method of approximate solution for the atomistic *N*-body wave mechanics problem. The basis for Hartree's model was the *independent particle approximation*, upon which Hartree was able to make intuitive arguments and write down equations for the wave-functions for the individual (non-interacting) electrons. To solve these equations, Hartree proposed a unique iterative procedure guided by *self-consistency*. Hartree's method was soon-after refined and generalized by J.C. Slater [2–4] and V.A. Fock [5] into what is known today as the Hartree-Fock (HF) method. The distinction between the Hartree and HF methods is an energy term called the *exchange energy*. The exchange energy term is the direct result of forcing the antisymmetry (Pauli exclusion) requirement on the many-body wave-function of the inhomogeneous electron gas. It is perhaps an irony that the Hartree method can often give better results than the more correct HF method. This is because of a convenient error cancellation between the exchange energy and the *correlation* energy, both of which—as we will soon see—are points of controversy in the world of electronic structure modelling.

The HF method has many advantages, not the least of which is the ability to systematically improve the accuracy by adding layers of complexity. The HF and post-HF methods are magnificently successful in predicting ground state (GS) and excited state properties of many species of atoms and small molecules; but the applications of HF methods are stringently limited by the number of electrons in the system. It became evident that computational models built on wave-functions were simply too numerically complex to be applied to systems with more than a few atoms. Luckily for the science community, physicists L.H. Thomas and E. Fermi had been independently developing a method in which the particle density instead of the wave-function was used to treat the quantum mechanical problem. From these roots we also see the early development of the *local density approximation (LDA)*—a step that would be vital to the later success of density functional theory (DFT). Thomas and Fermi used a LDA not only to for exchange and correlation energies, but also the kinetic energy. Unfortunately, the LDA of kinetic energy is rather severe, and limits the success of the Thomas-Fermi (TF) method to a few metals on the periodic table. For this reason, the notion of electron density found most of its popularity amongst the theoretical metallurgical community as a crude way of describing electronic structure.

For convenience, this chapter adopts the convention of Hartree atomic units (a.u.) in which the elementary electron charge e, electron mass m_e, Planck's constant $\hbar$, and Coulomb's law constant $(4\pi\varepsilon_0)^{-1}$ are all unity by definition.

1.1 Density Functional Theory

Around 1964, W. Kohn revisited the idea of electron density while studying the electronic structure of alloys. He began to wonder if it was possible to build a complete and precise description of electronic structure purely in terms of electron density. While on sabbatical in Paris, Kohn began working with P. Hohenberg (who at the time was also on sabbatical in Paris) and together they laid the theoretical framework to describe the inhomogeneous electron gas problem. In a landmark paper [6] Hohenberg and Kohn rigorously proved that the relationships do exist to define a stationary electron system by its GS density (i.e., the density which minimizes the total energy). Then, when Kohn returned home to the University of California at San Diego, he began working with L.J. Sham and together, formulated a set of self-consistent equations [7] which formed the basis for DFT and for which Walter Kohn was awarded the Nobel Prize in Chemistry in 1998.

In the sections that follow, a description will be given of the formal basis on which DFT was developed. Although DFT is not limited to atomistic problems, this description will proceed as such to explain DFT as it applies to a condensed aggregate of atoms. This is, after all, the spirit in which it was originally developed. The approach that follows is adapted from Refs 6–12, and references therein. Complete proofs and details can be found in those references.

The aim of DFT is to define the properties of an inhomogeneous electron gas. Consider a collection of N_{at} nuclei, with coordinates $\{\mathbf{R}_I\}$. Around them is a field of N electrons with coordinates $\{\mathbf{r}_i\}$. The electronic system constitutes a gas of interacting fermions which arrange themselves as to minimize the total energy of the system.

The large difference in mass between electrons and nuclei (in the order of 10^3 to 10^4 times) leads naturally to an adiabatic separation of their degrees of freedom. Hence, the electronic and nuclear subsystems—if the nuclear system is treated at all—are treated separately. For treatment of the electronic system, it is convenient to approximate the nuclei as infinitely massive points instead of quantum particles. The question then becomes entirely of how the electrons arrange themselves within the static Coulomb field of the nuclei as to achieve the energy minimum. To answer this question is to rigorously examine the

components of the energy and parametrize it in terms of some quantity which defines the behaviour of the electrons.

▰▰▰▰▰▰▮ **NOTA BENE**

In this and following sections I consider only non-spin polarized calculations. Spin polarization adds significant complexity to the problem, but is not necessary for materials which are not strongly influenced by these effects. Neither GaAs nor diamond (or its surfaces) require explicit consideration of spin polarization for accurate quantum mechanical descriptions.

1.1.1   Electron density

One of the possible parametrizations of the energy is in terms of the many-electron wave-function, $\Psi(\mathbf{r}_1, \mathbf{r}_2, \ldots, \mathbf{r}_N)$, of the system. This is the approach of many *ab-initio* procedures, most notably the HF and post-HF methods. DFT takes a slightly more direct route and allows us to write the total energy in terms of the density of the electrons which is a function of only a single coordinate, $\mathbf{r}$. The wave-function and particle density $n(\mathbf{r})$ are related:

$$n(\mathbf{r}) \equiv N \int \cdots \int \prod_{i=2}^{N} d\mathbf{r}_i \ |\Psi(\mathbf{r}, \mathbf{r}_2, \ldots, \mathbf{r}_N)|^2 \tag{1.1}$$

However, the act of squaring the wave-function removes a great deal of information that was once assumed vital to predicting the GS energy. As a simple example, take the case of an unbound electron, the wave-function of which is a complex plane-wave. The kinetic energy, T, associated with that plane-wave is related to its variation, $T \equiv \langle \psi | \frac{1}{2} \nabla^2 | \psi \rangle$, but the density will be *homogeneous*. So how can we determine the kinetic energy of the electrons from their density? As it turns out for this simple example, it is possible to find the relationship between density and kinetic energy; but if the problem were analytically intractable, this would certainly not be the case. Thomas and Fermi developed an approximate approach based on the local density of the electrons. The idea was that if the density varied slowly enough, you could take each volume element dV (Figure 1.2 on p. 13) and approximate the kinetic energy (and other quantities) in that volume with the corresponding values of the homogeneous gas problem at the same density. The LDA is a poor approximation since kinetic energy is a non-local quantity; that is, the kinetic energy in each volume element depends non-locally on density at every other point in space. This is why the TF method only works well for metals where the electron density is very smooth and the non-local dependency is relaxed.

6

1.1.2 Hohenberg and Kohn Theorems

A more general and precise approach to the problem than that of Thomas and Fermi came from Hohenberg and Kohn [6], and Kohn and Sham [7]. A formal method to rival that of Thomas and Fermi was not established until the Kohn-Sham (KS) paper, but the formal groundwork was laid in 1964 by Hohenberg and Kohn in a landmark paper proving two significant theorems:

Hohenberg-Kohn (HK) Theorem 1: The Uniqueness Principle. *The external potential $v(\mathbf{r})$ is uniquely determined by the ground state density $n(\mathbf{r})$ aside from a trivial constant.*

HK Theorem 2: The Variational Principle. *There exists a universal functional of density, $F[n(\mathbf{r})]$, which is not dependent on the external potential $v(\mathbf{r})$ such that the total energy*

$$E[n] \equiv \int d\mathbf{r} \, v(\mathbf{r})n(\mathbf{r}) + F[n], \tag{1.2}$$

is minimized when $n(\mathbf{r})$ has its correct ground state value corresponding to $v(\mathbf{r})$.

These theorems prove that the electron density can indeed be used to rigorously and precisely define GS properties of the system. If the potential is determined by the density, then the density maps one-to-one to a unique many-body wave-function, meaning (among other things) that the kinetic energy is indeed uniquely defined by the density. The two theorems together tell us that a complete Hamiltonian can be constructed from the electron density and the variational principle provides us with a foundation for a minimization scheme to solve for the electron density given an external potential.

The total energy can be written in terms of the wave-function as

$$E[\Psi] = \langle \Psi | v(\mathbf{r}) | \Psi \rangle + \langle \Psi | (T + U) | \Psi \rangle,$$

where U is the energy of electronic interaction. So, from Eq. (1.2) it can be seen that the universal functional $F[n]$ is a composition of several energy functionals since, by necessity, $F[n(\mathbf{r})] = \langle \Psi | (T + U) | \Psi \rangle$. The electronic interaction must contain the Coulomb interaction of the electrons, plus the effects of exchange and correlation. So, $F[n] = T_s[n] + E_{ee}[n] + E_{XC}[n]$ where $T_s[n]$ is our still unknown kinetic energy functional, E_{ee} is the Coulomb energy functional of the electrons and E_{XC} is the even more mysterious exchange-correlation energy functional. As a final step in the Hohenberg and Kohn discussion, we will consider $F[n]$ without E_{ee} under the definition

$$G[n] \equiv T_s[n] + E_{XC}[n]. \tag{1.3}$$

If we subscribe to the statistical interpretation of the wave-function, then it is an intuitive step to say that the density of charge in space ρ is proportional to the electron density, $\rho(\mathbf{r}) = -en(\mathbf{r})$, with electron charge e (which is unity in atomic units). It is then reasonable to evaluate the Coulomb interaction functional as

$$E_{ee}[n] = \frac{1}{2} \iint d\mathbf{r}d\mathbf{r}' \frac{n(\mathbf{r})\,n(\mathbf{r}')}{|\mathbf{r} - \mathbf{r}'|}, \tag{1.4}$$

where the double integral takes the interaction between all point pairs in space. The energy functional (Eq. (1.2)) then becomes

$$E[n] = \int d\mathbf{r}\, v(\mathbf{r})n(\mathbf{r}) + \frac{1}{2} \iint d\mathbf{r}d\mathbf{r}' \frac{n(\mathbf{r})\,n(\mathbf{r}')}{|\mathbf{r} - \mathbf{r}'|} + G[n]. \tag{1.5}$$

1.1.3 Self-Interaction Energy

Since $n(\mathbf{r})$ inseparably contains the density at $\mathbf{r}$ for every electron in the system, the double integral in Eq. (1.4) will include each particle's interaction with its own field. We know from the laws of electricity and magnetism that particles do not interact with themselves, so how can this be? This so-called self-interaction energy is supposed to be cancelled exactly by E_{XC}. As a point of comparison, the self-interaction within the HF formalism is exactly cancelled in the Slater exchange term. In DFT, the cancellation of the self-interaction energy is entirely dependent on our approximation of E_{XC}. Using LDA-based schemes in many cases can lead to self-energy cancellation to within a few percent, but this situation is worsened when $n(\mathbf{r})$ has sharp features which can lead to very strong self-energies.

1.1.4 The Kohn-Sham Equations

In 1965, Kohn and Sham explicitly demonstrated that the **ground state** many-electron problem can be exactly described by an equivalent set of single-particle self-consistent equations. This means that the ground state electron density of any given system can be expressed in terms of the wave-functions of a set of non-interacting pseudo[1]-particles. The proof lies simply in showing that the HK variational principle (page 7) applied to either the interacting or non-interacting systems leads to the same set of self-consistent equations. This proof is not shown here, but this section will follow the same approach as that presented in the original Kohn-Sham paper. This approach treats only the interacting problem, but a good treatment of the non-interacting problem can be found in Ref. 13.

---

[1] I call them *pseudo*-particles because they do not correspond to real particles. They simply have the same properties as the real particles under certain conditions.

Starting from Eq. (1.5), Kohn and Sham used the HK variational principle to find the GS density subject to the stationary condition

$$\frac{\delta E[n]}{\delta n} = 0,$$

which is analogous to finding the extrema of functions by setting the derivatives to zero. Applying this condition under the constraint

$$\int d\mathbf{r} \, \delta n(\mathbf{r}) = 0 \tag{1.6}$$

(conservation of N), Kohn and Sham obtained the equation

$$\int d\mathbf{r} \, \delta n(\mathbf{r}) \left\{ \varphi(\mathbf{r}) + \frac{\delta T_s[n]}{\delta n(\mathbf{r})} + \mu_{\mathrm{xc}}(n(\mathbf{r})) \right\} = 0, \tag{1.7}$$

where

$$\varphi(\mathbf{r}) = v(\mathbf{r}) + \int d\mathbf{r}' \, \frac{n(\mathbf{r}')}{|\mathbf{r} - \mathbf{r}'|} \tag{1.8}$$

and[2]

$$\mu_{\mathrm{xc}} = \frac{\delta E_{\mathrm{XC}}}{\delta n}. \tag{1.9}$$

Kohn and Sham then state that Equations (1.6) and (1.7) are identical with those obtained by applying the HK theorems to an equivalent system of non-interacting electrons in the potential $\varphi + \mu_{\mathrm{xc}}(n(\mathbf{r}))$ obeying the one-particle Schrödinger-like equation

$$\left[-\frac{1}{2}\nabla^2 + \varphi(\mathbf{r}) + \mu_{\mathrm{xc}}((n(\mathbf{r})) \right] \psi_i(\mathbf{r}) = \epsilon_i \psi_i(\mathbf{r}). \tag{1.10}$$

The term here in square brackets is called the Kohn-Sham Hamiltonian, H_{KS}, and the set of equations represented in Eq. (1.10) are called the Kohn-Sham equations. Now the density can be expressed in terms of the single-particle wave-functions as

$$n(\mathbf{r}) = \sum_{i=1}^{N_{\mathrm{occ}}} |\psi_i(\mathbf{r})|^2, \tag{1.11}$$

where the sum takes place over $\psi_i(\mathbf{r})$ corresponding to occupied states only. In Ref. 13, P. Giannozzi derives the KS equations starting from the single particle problem, showing this equivalence.

The non-interacting pseudo-electrons do in fact feel the average effect of each other by way of the integral term in Eq. (1.8). So the wave-functions used to construct $n(\mathbf{r})$ already depend on $n(\mathbf{r})$. This is why a self-consistent solution method is required.

---

[2]This expression for μ_{xc} is more general than the one given by KS, since they explicitly included the LDA in their equations.
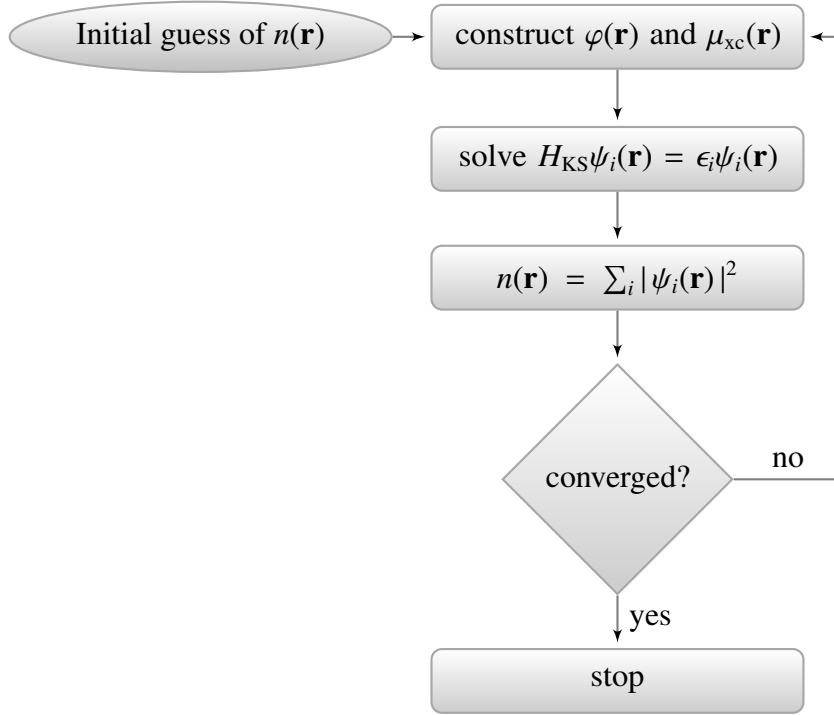
Figure 1.1: A flowchart illustrating a typical implementation of the self consistent cycle for DFT. The cycle is started with an initial guess at the density, then the potential and XC terms are constructed so that the KS equation can be solved for each electron. The KS wave-functions give a new density which is fed back to the beginning of the cycle until convergence criteria are met.

1.1.5   The Self-Consistent Cycle

Starting from some initial guess for $n(\mathbf{r})$, we can cyclically refine the shape of the density. This approach is necessary because the potential is dependent on the density. This makes the electron density a self dependent quantity. The cycle for solving this type of problem is illustrated in Figure 1.1. The cycle begins with the construction of the potential and XC terms from Eqs. (1.8) and (1.9). The next guess of $n(\mathbf{r})$ is constructed from the KS wave-functions found by solving the Kohn-Sham equations (Eq. (1.10)). The new density is then calculated from the KS wave-functions with Eq. (1.11) and is subsequently fed back to the beginning of the cycle where the potential and XC terms are recalculated. As successive density functions approach the GS, they will vary less and less from one cycle to the next. This convergent behaviour is monitored to determine whether or not $n(\mathbf{r})$ is a sufficient approximation to the true GS density.

The total KS energy is typically used as a criterion for convergence. While it is not the only possible criterion, it is convenient because the HK variational principle assures us in a

very precise way that as $n(\mathbf{r})$ approaches the true GS density, $n_0(\mathbf{r})$, the energy of the system will approach its global minimum. More concisely, $\delta E[n]/\delta n \longrightarrow 0$ as $n \longrightarrow n_0$. While it is necessary that the first order variation of $E[n]$ approaches zero as the density approaches its ground state, the complimentary statement is not. Care must be taken to avoid trapping the system within metastable regions of the electronic energy surface, but this is not generally a problem in modern implementations of the theory.

1.1.6 The Total Energy Functional

To write the total energy, we start once again with Eq. (1.5) and expand the functional $G[n]$ with its definition in Eq. (1.3):

$$
\begin{aligned}
E[n] &= \int d\mathbf{r}\, v(\mathbf{r})n(\mathbf{r}) + \frac{1}{2} \iint d\mathbf{r}d\mathbf{r}'\, \frac{n(\mathbf{r})\,n(\mathbf{r}')}{|\mathbf{r} - \mathbf{r}'|} + T_s[n] + E_{\mathrm{XC}}[n] \\
&= T_s[n] + \int d\mathbf{r}\, v(\mathbf{r})n(\mathbf{r}) + \frac{1}{2} \iint d\mathbf{r}d\mathbf{r}'\, \frac{n(\mathbf{r})\,n(\mathbf{r}')}{|\mathbf{r} - \mathbf{r}'|} + E_{\mathrm{XC}}[n].
\end{aligned}
\tag{1.12}
$$

From this, we only need to expand $T_s[n]$ and $E_{\mathrm{XC}}[n]$ in order to have a closed form expression for the total energy. As we discussed earlier, the kinetic energy term has historically been an obstacle to density methods. The density contains no direct information about the curvature of the wave-function and therefore, no direct information about the kinetic energy. We do know from the HK uniqueness theorem that the GS density does uniquely define the kinetic energy because the GS density maps one-to-one with the GS wave-function. However, this leaves us with no clear approach to find the kinetic energy directly from the GS density. DFT avoids this problem altogether since the kinetic energy can indeed be calculated from single particle wave-functions. Kohn and Sham have demonstrated the equivalence of the interacting and non-interacting ground state problems, so it is possible (and equivalent) to simply find and sum the single-particle kinetic energies and by-pass the need for a direct functional $T_s[n]$. So the kinetic energy of the interacting problem is then

$$
T_s[n] = T_s[\{\psi_i\}] = \frac{1}{2} \sum_i \int d\mathbf{r}\, \psi_i^* \nabla^2 \psi = \frac{1}{2} \sum_i \langle \psi_i | \nabla^2 | \psi_i \rangle,
\tag{1.13}
$$

leaving us with the expression for total energy

$$
E[\{\psi_i\}] = \frac{1}{2} \sum_i \langle \psi_i | \nabla^2 | \psi_i \rangle + \int d\mathbf{r}\, v(\mathbf{r})n(\mathbf{r}) + \frac{1}{2} \iint d\mathbf{r}d\mathbf{r}'\, \frac{n(\mathbf{r})n(\mathbf{r}')}{|\mathbf{r} - \mathbf{r}'|} + E_{\mathrm{XC}}[n].
\tag{1.14}
$$

The exchange-correlation energy term is all that is left to find the total energy of the electronic system. All of our error—and our current ignorance—is kept in the XC term

11

which has been and is currently an open area of research. As of now, nobody has published a closed form expression for the real $E_{XC}[n]$. Progress in this area of research is slow and many scientists believe that no tractable expression for the true form of E_{XC} exists. Many approximations are available but most have a limited scope of usefulness. The most widely applicable approximations are based strongly on LDA and a Taylor-like series expansion of its gradient terms, which will be discussed in the next section.

Equation (1.14) can be used to guide the self-consistent process of solving for $n(\mathbf{r})$ using the KS equations. It encompasses all of the energy of the electron system in its ground state. As one final point, it is often useful to include the energy of the nuclear Coulomb interactions, E_{nn}, in the expression for total energy. In terms of self-consistent iteration it is redundant, but for many investigations it is necessary to include geometrical considerations in the total energy. For example, if one wishes to find the minimum energy structure of a molecule or solid, electronic information is not enough to make a determination. This leads to our complete and final expression for the total energy of the atomic aggregate:

$$E[\{\psi_i\}] = \frac{1}{2} \sum_i \langle \psi_i | \nabla^2 | \psi_i \rangle + \int d\mathbf{r} \, v(\mathbf{r}) n(\mathbf{r})$$
$$+ \frac{1}{2} \iint d\mathbf{r} d\mathbf{r}' \, \frac{n(\mathbf{r})n(\mathbf{r}')}{|\mathbf{r} - \mathbf{r}'|} + E_{XC}[n] + E_{nn}(\{\mathbf{R}_I\}). \quad (1.15)$$

1.2   Exchange-Correlation Functionals

As stated earlier, the exact form for a universal exchange-correlation functional of density, $E_{XC}[n] = E_X[n] + E_C[n]$ is not known. It is the only approximation required within the density functional formalism, so it is of great importance that it be handled with care and deliberation. As such, it is the topic of great controversy and an active area of research. Many approximations for the exact functional exist. The most common measure of the quality of these approximations is conformity to the known behaviour of the exact exchange-correlation functional. This is often a matter of balance; while some approximations are better for some particular cases, they may fail for others.

The most practical of the XC functionals are typically centred around LDA and generalized gradient approximation (GGA). Some functionals incorporate the exact exchange obtained by HF theory (using the KS orbitals) or empirical quantities; and a broader class of functionals is a linear combination of all of these (hybrid functionals).

For the research presented herein, we employ only straightforward LDA and the GGA of Perdew, Burke and Ernzerhof (PBE). These functionals are briefly described in the two
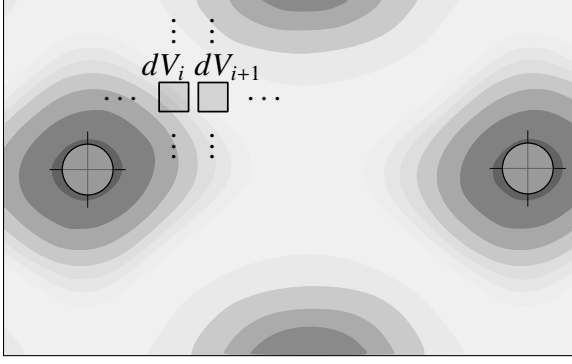
Figure 1.2: Under the local density approximation, the XC contribution of each element dV_i can be approximated by the corresponding values of the interacting homogeneous gas problem. This figure simply illustrates the elements overlaid with the contours of particle density.

subsections which follow.

The descriptions of LDA and GGA which follow consider the density $n(\mathbf{r})$ which is non-spin polarized. The descriptions are adapted from their more general counterparts wherein $n(\mathbf{r}) = n_\uparrow(\mathbf{r}) + n_\downarrow(\mathbf{r})$, is the sum of separate spin-up and spin-down densities. This is the convention likely to be encountered by the reader if they explore the references.

1.2.1 Local Density Approximation

The local density approximation was partly described earlier in §1.1.1 where Thomas and Fermi used it to approximate the kinetic energy of a density field. The concept of LDA for the XC functional is similar. The core concept of the local density approximation is to remove all non-locality of the E_{XC} functional by approximating the exchange-correlation energy per particle at each volume element dV_i (see Figure 1.2) as the exchange-correlation of the interacting homogeneous gas. This means that the XC contribution from each element is independent of all other elements, making the XC a completely local quantity.

The exchange-correlation energy per particle of a homogeneous electron gas, $\epsilon_{XC}^{unif}(n)$, can be solved numerically, and has been conveniently parameterized by Perdew and Zunger [13, 14]. So we write the LDA exchange-correlation functional as

$$E_{SC}^{LDA}[n] = \int d\mathbf{r} \; n(\mathbf{r}) \; \epsilon_{XC}^{unif}(n(\mathbf{r})).$$

The local density approximation performs surprisingly well even for highly inhomogeneous systems for which a local approximation may be highly suspect. This is because it implicitly obeys several symmetry properties of the exact functional. Also, there is a convenient cancellation of errors between the exchange and correlation contributions to the functional. As one may expect, the results improve for systems with slowly varying density. But because of incomplete cancellation of the self energy (see §1.1.3), LDA allows Coulomb repulsion

to dominate resulting in delocalization of the density field [14–19]. Overall, LDA tends to over-bind causing over-estimates of cohesive energies and bond-lengths. In solid state, LDA has also been linked to a very serious underestimation of bandgaps by 40 to 100%.

1.2.2 Generalized Gradient Approximation

Similar to LDAs, GGAs also follow a pointwise application to individual volume elements, so GGAs are also a local approximation. The form for the XC term in GGAs is

$$E_{SC}^{GGA}[n] = \int d\mathbf{r} \, n(\mathbf{r}) \, f(n(\mathbf{r}), \boldsymbol{\nabla} n(\mathbf{r})). \quad (1.16)$$

The form of f is not so clear as in the LDA case. For our calculations, we use the PBE formulation [20]. What is clear from Eq. (1.16) is that we not only have dependence of local XC energy on $n(\mathbf{r})$, but also the spatial gradient $\boldsymbol{\nabla} n(\mathbf{r})$. The inclusion of gradient terms is not as straightforward as a simple Taylor expansion. Such simple expansions do not obey the symmetry principles to which the exact XC functional is known to conform.

In comparison with LDAs, GGAs tend to soften and broaden bonds which improves total energies, energy barriers and structural predictions. As with LDAs, GGAs have their successes and weaknesses. In some cases, they correct problems associated with LDAs, and in other cases they over-correct LDA predictions.

1.3 DFT on a Crystal Lattice

Solids present a distinct problem from that of individual atoms or molecules, where the properties depend on dozens or even hundreds of electrons. Indeed, the properties of bulk solids are resultant from the behaviour of a continuum of atoms distributed across macroscopic volumes culminating in numbers of electrons many orders of magnitude higher than these other cases. The periodicity of crystal lattices does however allow us to consider only a small volume (the supercell) which is periodically repeated *ad infinitum*, leading to a finite set of single-particle equations subject to translational symmetry. Obviously, this is not an approximation which is safely made for amorphous or otherwise non-crystalline solids.

The propagation of the cell through infinite space is mathematically achieved through the application of periodic boundary conditions. These conditions, along with the cell geometry (and symmetry) shape the reciprocal space of the lattice. The reciprocal lattice vectors $\mathbf{G}$ are those which satisfy the relationship $\exp[i\,\mathbf{G} \cdot \mathbf{l}_a] = 1$ where $\mathbf{l}_a$ is a lattice vector of

the crystal. For an infinite lattice defined by primitive vectors $\{\mathbf{a}_1, \mathbf{a}_2, \mathbf{a}_3\}$, the primitive reciprocal lattice vectors $\{\mathbf{g}_1, \mathbf{g}_2, \mathbf{g}_3\}$ are

$$\mathbf{g}_1 = 2\pi \frac{\mathbf{a}_2 \times \mathbf{a}_3}{\mathbf{a}_1 \cdot (\mathbf{a}_2 \times \mathbf{a}_3)},$$

$$\mathbf{g}_2 = 2\pi \frac{\mathbf{a}_3 \times \mathbf{a}_1}{\mathbf{a}_1 \cdot (\mathbf{a}_2 \times \mathbf{a}_3)},$$

and

$$\mathbf{g}_3 = 2\pi \frac{\mathbf{a}_1 \times \mathbf{a}_2}{\mathbf{a}_1 \cdot (\mathbf{a}_2 \times \mathbf{a}_3)}.$$

Reciprocal space provides mathematical convenience due to its relationship to momentum and Fourier space. Many calculations are performed efficiently in the space of the reciprocal lattice. In these cases, it is convenient to define the primitive cell of reciprocal space constructed from $\{\mathbf{g}_1, \mathbf{g}_2, \mathbf{g}_3\}$ called the Brillouin zone (BZ). In the BZ, symmetry becomes less abstract and many calculations can be made efficient with proper sampling of momentum ($\mathbf{k}$)-points within the BZ. The density of $\mathbf{k}$-points is proportional to the volume of the cell since the volume of the BZ is inversely proportional to the volume of the real cell.

1.3.1 Bloch Theorem

The imposition of translational symmetry on the electronic wave-functions makes them subject to Bloch's theorem. From Kittel [21]:

Bloch's Theorem. *The eigenfunctions of the wave equation for a periodic potential are the product of a plane-wave* $\exp(i\,\mathbf{k} \cdot \mathbf{r})$ *times a function* $u_\mathbf{k}(\mathbf{r})$ *with the periodicity of the crystal lattice.*

Bloch's theorem allows us to write the wave-function of an electron in a periodic potential as the product of cell-periodic part and a wave-like part:

$$\psi_\mathbf{k} = u_\mathbf{k}(\mathbf{r})\, e^{i\mathbf{k}\cdot\mathbf{r}}$$

The cell-periodic part can be expanded as a discrete series of plane-waves, the wave-vectors of which are reciprocal lattice vectors:

$$u_i(\mathbf{r}) = \sum_\mathbf{G} c_i \exp[i\mathbf{G} \cdot \mathbf{r}].$$

Therefore, each electronic wave-function in a band with index i can also be expanded on a basis of plane-waves,

$$\psi_{i,\mathbf{k}}(\mathbf{r}) = \sum_{\mathbf{G}} c_{i,\mathbf{k}+\mathbf{G}} \exp[i(\mathbf{k} + \mathbf{G}) \cdot \mathbf{r}].$$

███████▮ **NOTA BENE**

Beware of the ambiguity of band index i and the imaginary unit i. Context should distinguish these two cases clearly. Logically, the index will appear in subscripts and the imaginary unit will appear as a term or factor.

Electronic states are confined to a set of **k**-points within the BZ. Only a finite number of wave-functions are occupied at each **k**-point, but an infinite sampling of the BZ is required to exactly describe the density (or any other quantity which requires integration over the BZ). However, the wave-functions and eigenvalues may not be significantly different from one **k**-point to the next, so a discrete sampling of the BZ is a good approximation. As the eigenvalues change as a function of **k**, they are said to disperse through the BZ. Smaller BZs corresponding to larger cells require less sampling because there is a smaller volume restricting dispersion. Error due to inadequate **k**-sampling can always be reduced by increasing the sampling mesh density. Total energies will converge as the **k**-mesh density approaches a sufficient level.

1.4 Plane-Wave Pseudopotential Method

The plane-wave pseudopotential method is one of the most commonly used for DFT simulations in solids. It is an extension of DFT based upon a series of approximations and symmetry arguments which work well in periodic solids. The method takes advantage of periodicity and Bloch's theorem with a simple plane-wave basis set, but practical restrictions on the size of the basis set call for the pseudopotential approximation (§1.4.2) to remove some complexity from the wave functions.

1.4.1 Plane-Wave Basis

Bloch's theorem (§1.3.1) allows the electronic wave-functions to be expanded on a discrete basis of plane-waves. In principle, this basis is countably infinite. Larger values of **k** correspond to electrons with higher kinetic energy $(\hbar^2/2m_e)\,|\mathbf{k} + \mathbf{G}|^2$. DFT being a ground state theory, it is reasonable that the electronic wave-functions are well expressed with
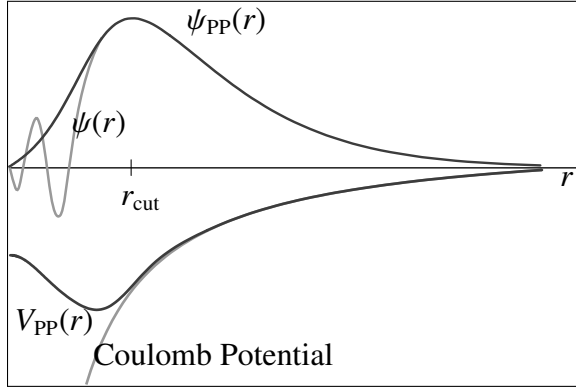
Figure 1.3: A comparison of the pseudopotential V_{PP} (black line) with the Coulomb potential (grey line) and resultant wave-functions. The real wave-function (grey line) undulates while the PP wave-function (black line) rises and falls off. This data was taken from a local PP for Arsenic.

a truncated basis set containing plane-waves below a certain cut-off energy E_{cut}. More concisely, the Fourier-like plane-wave coefficients, $c_{i,\mathbf{k+G}}$, should become negligible after a certain $\mathbf{k}_{cut}$ which corresponds to energy that is typically higher than the energies of the electrons. If E_{cut} begins to remove non-negligible coefficients from the basis, then error becomes significant. Total energies will converge as E_{cut} is increased, so one can always manage and reduce errors associated with the size of the plane-wave basis set.

1.4.2 Pseudopotentials

The steep Coulomb potential near the ion cores undulates the electronic wave-functions near those regions. These undulations are necessary to satisfy orthogonality between the wave-functions. The sharpness of the resultant wave-function peaks increases with the steepness of the potential. These sharp features demand a larger basis set, taxing the physical memory of the computers on which the calculations are performed and the patience of those who await the results.

The wave-functions of the core (non-valence) electrons are insensitive to changes at the valence level. These core states are bound very deeply in the potential well of the nuclei. Computational complexity is reduced considerably if only the valence electrons are considered. To facilitate this, the nuclei and core electrons can be amalgamated into a single potential well, against which the valence electrons are scattered. This approximation is only viable under the caveat that the wave-functions of the valence electrons in the *pseudopotential* of the nuclei+core electrons must be identical to the real valence wave-functions after some cut-off radius r_{cut}. The pseudopotential (PP) wave-functions, in contrast to the real ones, have no high-frequency undulations near the core (see Figure 1.3).

Softer PPs have smoother wave-functions requiring a smaller basis set. Ideally, PPs are constructed so that their scattering properties are identical to the nucleus+core after the

17

radius r_{cut} but the resulting pseudo wave-functions have no radial nodes. The calculation of PPs is a science and art unto itself. Many PPs are available in libraries or collections produced by researchers. There are many methods, variants and varieties of PPs and PP formulas. Knowing the differences and consequences of each is important.

Locality of the PP is of particular importance. Electrons may scatter off of the pseudopotential differently depending on their angular momentum component l. A local PP does not account for this fact and every electron, regardless of angular momentum feels the same pseudo-potential. In non-local PPs, a different potential is specified for each l of the ground state valence configuration. The most general form for a non-local PP is

$$V_{NL} = \sum_{lm} |lm\rangle V_l \langle lm|,$$

where $|lm\rangle$ are spherical harmonics which decompose the wave-functions into angular momentum components (with angular momentum l and spin m) and V_l is the PP corresponding to angular momentum l. Local PPs have no decomposition of spherical harmonics, so only a singular potential is felt by all electrons. Local PPs are simpler and faster for calculations, but are less accurate. Non-local PPs improve accuracy at the cost of computational simplicity.

1.4.3   Quantum ESPRESSO

From the Quantum ESPRESSO website (http://www.quantum-espresso.org/),

> Quantum ESPRESSO is an integrated suite of computer codes for electronic-structure calculations and materials modelling at the nanoscale. It is based on density-functional theory, plane-waves, and pseudopotentials (both norm-conserving and ultrasoft).

Quantum ESPRESSO release versions 3.2.3 is the computer code used for all molecular dynamics (MD) calculations for the research presented herein. The PPs used were available on the Quantum ESPRESSO website under the names `As.gon.UPF`, `C.pz-vbc.UPF` and `Ga.pz-bhs.UPF`.

1.5   Augmented Plane-Waves With Local Orbitals

The augmented plane-wave with local orbitals (APW+lo) [22] is a logical extension of Slater's augmented plane-wave (APW) [23] basis and the more recent (and successful)

linearised augmented-plane-wave (LAPW) [24] basis. DFT methods employing the APW+lo basis set are among the most accurate methods for crystals. All points in the cell are divided into one of two regions: (M) non-overlapping spherical regions called the muffin tin (MT) regions, concentrically located at atomic sites and (I) everything not inside the MT spheres, i.e., the interstitial regions connecting the spheres. The APW basis set consists of plane-waves in the interstitial region that are augmented into radial solutions of the Schrödinger equation $u_l(r, E)$ inside the MT spheres:

$$\phi_{\mathbf{k+G}}^{\text{APW}}(\mathbf{r}) = \begin{cases} \frac{1}{\sqrt{\omega}} \exp\left[i\left(\mathbf{k + G}\right) \cdot \mathbf{r}\right] & \text{for} \quad \mathbf{r} \in I \\ \sum_{lm} A_{lm,\mathbf{k+G}}\, u_l(r, E_l)\, Y_{lm}(\hat{\mathbf{r}}) & \text{for} \quad \mathbf{r} \in M \end{cases} \tag{1.17}$$

where Y_{lm} are spherical harmonics of angular momentum and spin coordinates lm, and $A_{lm,\mathbf{k+G}}$ are the respective coefficients. The radial Schrödinger functions describe the sharp features of the core electrons where the plane-wave basis would require a prohibitively large number of plane-waves. The radii of the MT spheres—the so called *muffin tin radii*—are chosen so that they contain the core electrons leaving the valence electrons in the interstitial region. The wave-functions of the valence electrons in the interstitial regions are much smoother and are well described by the plane-waves. Of course, the values and derivatives must match at the boundary surfaces swept by the MT radii.

The basis functions in the MT regions are lacking in variational flexibility. To add extra flexibility, additional $\mathbf{k + G}$–independent basis functions can be added to the set. The so-called *local orbitals (lo)* consist of a linear combination of two radial functions (at two different energies) and one energy derivative (at one of the two energies):

$$\phi_{lm}^{\text{lo}}(\mathbf{r}) = \begin{cases} 0 & \text{for} \quad \mathbf{r} \in I \\ \left(A_{lm}^{\text{lo}}\, u_l(r, E_{1,l}) + B_{lm}^{\text{lo}}\, \frac{du_l}{dE}\Big|_{(r,E_{1,l})}\right) Y_{lm}(\hat{\mathbf{r}}) & \text{for} \quad \mathbf{r} \in M \end{cases} \tag{1.18}$$

These additions maintain orthogonality by allowing the treatment of the semi-core and valence states within a single energy window. The local orbitals are normalized and have zero slope and value at the muffin tin radii.

The bases in Eqs. (1.17) and (1.18) are summed into a single basis $\phi_{\mathbf{k+G}}^{\text{APW+lo}}$ and the wave-functions are then expanded on the combined APW+lo basis:

$$\psi_i(\mathbf{r}) = \sum_{\mathbf{G}} c_{i,\mathbf{k+G}}\, \phi_{\mathbf{k+G}}^{\text{APW+lo}}(\mathbf{r}).$$

The coefficients $c_{i,\mathbf{k+G}}$ are solved via non-linear optimization techniques.

Compared to a completely plane-wave basis with pseudopotentials, the APW+lo basis is much more accurate, but it does however come at the cost of simplicity. Not only is the

APW+lo basis conceptually more complicated, it is dependent on atomic coordinates; i.e., the basis must be constructed to suit each individual configuration of atoms. This limits the usefulness of APW+lo methods in cases where the atoms must be continually moved, such as structural optimization and molecular dynamics.

As a final note, a similar parameter to that of the cut-off energy for the plane-wave pseudopotential method exists for the full-potential linearised augmented-plane-wave (FP-LAPW)/APW+lo schemes as well. For these basis sets, the product of the smallest muffin tin radius and the magnitude of the largest **k**-vector, $R_{MT} K_{max}$, determines the size of the basis.

1.5.1   WIEN2k

From the WIEN2k website (http://www.wien2k.at/):

> The program package WIEN2k allows to perform electronic structure calculations of solids using density functional theory (DFT). It is based on the full-potential (linearized) augmented plane-wave ((L)APW) + local orbitals (lo) method, one among the most accurate schemes for band structure calculations. WIEN2k is an all-electron scheme including relativistic effects and has many features. It has been licensed by more than 1350 user groups.

The WIEN2k manual [25] contains minimal theory, but has many references to form the theoretical basis of the software.

WIEN2k was used for all of the calculations of optics and density of states (DOS) for GaAs.

1.6   *Ab-Initio* Molecular Dynamics

Ab initio molecular dynamics is a method for finding atomic trajectories subject to forces calculated by a first principles treatment of the electronic structure. DFT is most often used for the electronic structure calculations while the ions are propagated classically according to Newton's equation of motion. To obtain the forces on the ions, the so called Hellman-Feynman theorem is invoked. Adiabatic separation of electronic and ionic time scales is a necessary exploit. To a good approximation, the electrons relax to ground state almost instantaneously as the ions move through their trajectories. The potential energy surface in which the electrons remain in ground state is known as the Born-Oppenheimer

surface. The Born-Oppenheimer molecular dynamics (BOMD) scheme as described in §1.6.2 holonomically confines the system to this surface at the expense of computational simplicity. The Car-Parrinello molecular dynamics (CPMD) scheme is much less computationally demanding, but runs the danger of leaving the Born-Oppenheimer (BO) surface. For a thorough introduction to the topic, see Ref. 26 and references therein.

1.6.1 Car-Parrinello Molecular Dynamics

The Car-Parrinello [27] approach to MD takes advantage of the adiabatic time-scale separation between the electrons and nuclei. It casts the dynamics of both systems into a simultaneous classical Lagrangian. The Car-Parrinello (CP) Lagrangian leads to a dynamics for electronic, ionic and cell parameters. For this brief subsection, the original approach of Car and Parrinello in Ref. 27 is followed. For a more detailed study, I would once again direct the reader to Ref. 26.

Previously, we have considered DFT with the parameters $\{\psi_i\}$ and $\{\mathbf{R}_i\}$ for single-particle orbitals and atomic centres respectively. In the CP approach, external constraints associated with the coordinates $\{\alpha_\nu\}$ are also evolved. In the same spirit as in §1.1.6, we write the total energy functional,

$$E[\{\psi_i\}, \{\mathbf{R}_I\}, \{\alpha_\nu\}] = \sum_i \int_\Omega d\mathbf{r} \, \psi^*(\mathbf{r}) \left[\frac{-\hbar^2}{2m_e} \nabla^2 \right] \psi_i(\mathbf{r}) + U(n(\mathbf{r}), \{\mathbf{R}_I\}, \{\alpha_\nu\}), \qquad (1.19)$$

which includes the energy associated with the constraints $\{\alpha_\nu\}$. Here, we also see that the familiar kinetic energy term is now integrated over the cell volume Ω. The parameters of the functional Eq. (1.19) are considered to be time dependent, and the Lagrangian

$$\mathcal{L}_{CP} = \frac{1}{2} \sum_i \mu \int_\Omega d\mathbf{r} \, |\dot{\psi}_i|^2 + \frac{1}{2} \sum_I M_I \dot{\mathbf{R}}_I^2 + \frac{1}{2} \sum_\nu \mu_\nu \dot{\alpha}_\nu^2 - E[\{\psi_i\}, \{\mathbf{R}_I\}, \{\alpha_\nu\}] \qquad (1.20)$$

is introduced, where μ is the mass associated with the classical *fictitious* electron dynamics, M_I are the masses of the nuclei and μ_ν are the masses associated with the fictitious dynamics of the constraints on the cell. Note, we use the familiar *dot* (˙) notation as usual to indicate time differentiation. The ψ_i in Eq. (1.20) are subject to orthogonality constraints

$$\int_\Omega \psi_i^*(\mathbf{r}, t) \psi_j(\mathbf{r}, t) = \delta_{ij}. \qquad (1.21)$$

The Lagrangian Eq. (1.20) is minimized under the constraints in Eq. (1.21) to give the

equations of motion for the system:

$$\mu \ddot{\psi}_i(\mathbf{r}, t) = -\frac{\delta E}{\delta \psi_i^*(\mathbf{r}, t)} + \sum_k \Lambda_{ik} \psi_k(\mathbf{r}, t), \tag{1.22}$$

$$M_I \ddot{\mathbf{R}}_I = -\boldsymbol{\nabla}_{\mathbf{R}_I} E, \tag{1.23}$$

$$\mu_\nu \ddot{\alpha} = -\frac{\partial E}{\partial \alpha_\nu}. \tag{1.24}$$

These equations are worth some discussion since there are some very interesting concepts in play.

Most notable of these concepts are the fictitious electron dynamics in Eq. (1.22), which propagate the wave-functions classically under *force* towards the minimum of E, originating from the functional derivative of energy with respect to the wave-functions $\psi_i^*(\mathbf{r}, t)$. These dynamics are void of any physical meaning, and are simply a mathematical means to an end. The sum term in Eq. (1.22) with the Lagrange multipliers Λ_{ik}, enforces the constraints in Eq. (1.21). Under equilibrium conditions ($\ddot{\psi}_i = 0$), the eigenvalues of Λ matrix are the occupied KS eigenvalues and Eq. (1.22) is equivalent to the KS Eqs. (1.10). Only in this case is the Lagrangian in Eq. (1.20) representative of the real physical system on the BO surface.

A simple test to be sure that the dynamics remain on the BO surface is to monitor the fictitious kinetic energy of the electron dynamics $K_e = \sum_i \mu \int_\Omega |\dot{\psi}_i|^2/2$. If $\ddot{\psi}_i$ remains equal to zero during the dynamics, then the fictitious velocities $\dot{\psi}_i$ will remain at zero. If the fictitious electron dynamics gain kinetic energy then the wave-functions must be relaxed back to the GS. If this procedure must be done frequently, it most often indicates an energy transfer from the ionic degrees of freedom to the electronic ones. This happens when there is an overlap of the vibrational spectra of the electrons and ions indicating a violation of the adiabatic assumption. Usually this is fixed by adjusting the fictitious electron mass μ to shift the spectrum of the electrons.

The dynamics of the cell constraints $\{\alpha_\nu\}$ in Eq. (1.23) are also fictitious. Often, these dynamics are ignored altogether, leaving only the traditional integration of the ions and electrons. The constraints can be useful, however if one wishes any parameters of the cell, such as volume or shape, to vary in time and be subject to the force of energy minimization. The masses μ_ν control the variational resistance of the degrees of freedom of the cell.

Finally, the ion dynamics in Eq. (1.24) are what one may traditionally expect. The propagation of the ions is indeed real, corresponding to the actual trajectories of the ions. The one caveat of the ion dynamics is that the integration time step is considerably finer than that required for coherent integration of the ionic equations of motion. This is because

of the simultaneous integration of ionic and electronic equations. In this particular instance, the usually helpful adiabatic condition resultant from the separation of ionic and electronic time-scales forces us to use an integration time step which correctly paces the evolution of the electrons.

1.6.2 Born-Oppenheimer Molecular Dynamics

BOMD approach is somewhat more straightforward than CPMD. In BOMD, the time dependence of the electronic structure is a direct consequence of ionic evolution. There is no active propagation of the orbitals. Instead, the time-independent ground state electron problem is solved for each ionic time step in the potential field cast by the fixed (or *clamped*) nuclei. The static electronic structure is used to calculate the forces on the ions at each time step, so the ionic equations of motion can be integrated on a time scale much larger than what is allowed in CPMD. The equations which define the dynamics are

$$M_I \mathbf{R}_I = -\frac{\delta E}{\delta n(\mathbf{r})}$$

$$H_{KS} \psi_i = \epsilon_i \psi_i.$$

THE TEMPERATURE DEPENDENT DIELECTRIC FUNCTION OF GALLIUM ARSENIDE: THEORY VS. EXPERIMENT

EXPERIMENTAL techniques based on optical response yield a wealth of information about the fundamental properties of materials. Optical properties of materials provide useful information concerning the bands structure and lattice modes of the material. Moreover, they can be used to probe for impurities and defects within the lattice. These measurements can typically be made without any deleterious effect on the sample. Thus, optical techniques are commonly used for non-invasive *in situ* monitoring of material growth and reactions at surfaces and interfaces [28].

Our current understanding of temperature dependent optical properties of materials is based mainly on experimental observation. Theoretical modelling of such properties has been a formidable problem in solid state physics for some time. The primary barriers to success are twofold; the ideal lattice and the independent particle approximations in electronic structure theory both fail to capture the essential physics of the problem. The optical properties of semiconductors are known to be strongly influenced by lattice dynamics. This influence is simply eliminated by the ideal lattice approximation wherein the nuclear sites are frozen in the ideal (minimum energy) configuration. Furthermore, effects of many body interactions become pronounced in semiconductors when their electrons are excited to higher energy states. The so called excitonic effects, i.e., the interactions of the excited electrons with their corresponding positive charge holes, are particularly strongly expressed in optical response measurements. These many-body effects are extinguished in the independent particle approximation, which is at the core of DFT. While efforts

continue to extend formalisms such as DFT to include many body effects, particularly with the successful *GW* approximation [29–31], little progress has been made in modelling the dynamical effects until recently [32].

In Ref. 32, we performed DFT based *ab-initio* molecular dynamics (AIMD) simulations on an eight atom cubic unit cell of GaAs, and the resultant MD trajectories were discretely sampled for calculations of optical properties. Each trajectory was characteristic of a different temperature in the range of 100 K to 700 K. Eight configurational *snapshots* were sampled along each trajectory. The optical properties of these snapshots were averaged, and an ergodic ansatz was used to establish the equivalence of the average over smaller samples with a larger sample. For temperatures below 700 K, this method yielded satisfactory results when compared to experimental data (particularly with the imaginary part of the complex linear optical dielectric function). However, at temperatures above 700 K, it becomes clear that the small size of the unit cell restricts Fourier components of the lattice potential causing *spurious* band shifts. These shifts result in unphysical transitions near the band-edge, hence creating artefacts in the complex dielectric function (see §2.1.1).

It is the goal of the research presented herein to extend the results to higher temperatures by considering a sixty-four atom cubic unit cell, which does not significantly restrict the Fourier components of the potential at that temperature. In addition, the sixty-four atom unit cell is exactly eight times the volume of the eight-atom cell. This relaxes our dependence on ergodicity and requires us to sample the optics of only a single configuration along a given MD trajectory.

2.1   Theoretical Background

This section provides a basis for interpreting the results of the calculations presented in this chapter. The key concepts are the physical definition of the complex dielectric function, the effects of lattice distortions on electronic structure, the nature and consequences of thermal expansion and the distinction between MD temperature and empirical temperature.

2.1.1   Optical Calculations

The complex dielectric function $\varepsilon(\omega)$ is related to electronic band structure. And so, many applications of GaAs depend on this function making it an abundant source of information about the material. It summarizes the interband transition processes which take place at various points in the BZ. The conventional cell of GaAs can be resolved into two overlapping
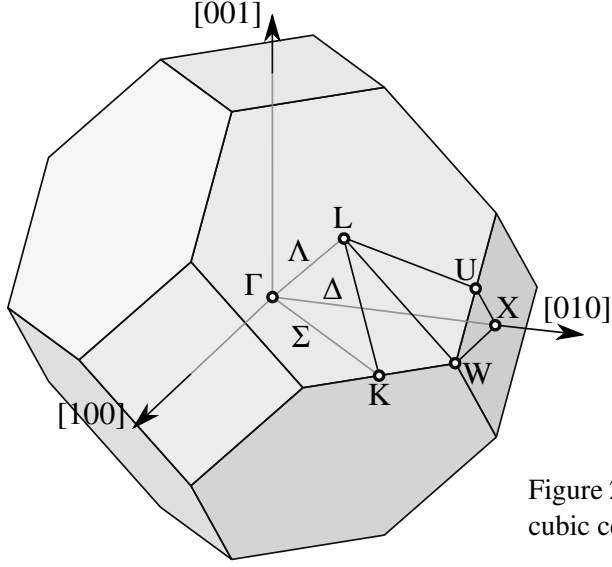
Figure 2.1: The first Brillouin zone for the face-centred cubic cell with high symmetry points and lines labeled.

face centred cubic (FCC) conventional cells, displaced by the lattice vector $[\frac{1}{4}\ \frac{1}{4}\ \frac{1}{4}]$. The BZ of of GaAs (Figure 2.1) therefore belongs to a FCC lattice.

Despite its close relationship to quantum mechanics, the complex dielectric function has its roots in classical electrodynamics. The propagation of light through a linear material is determined largely by the complex linear optical dielectric tensor [33]. In a linear homogeneous medium, the displacement field **D** is related to the imposed electric field **E** by

$$\mathbf{D}(t) = \varepsilon_0 \bar{\varepsilon}(\omega) \wedge \mathbf{E}(t)$$

where $\wedge$ indicates tensor-vector multiplication and $\bar{\varepsilon}(\omega)$ is the complex dielectric tensor dependent on frequency ω of the time-dependent electric field (or more accurately, photon frequency). The cubic symmetry of GaAs imposes isotropic symmetry on the tensor:

$$\bar{\varepsilon}(\omega) = \begin{pmatrix} \tilde{\varepsilon}_{xx}(\omega) & 0 & 0 \\ 0 & \tilde{\varepsilon}_{xx}(\omega) & 0 \\ 0 & 0 & \tilde{\varepsilon}_{xx}(\omega) \end{pmatrix}$$

Here, the tildes over the epsilons remind us that each element of the tensor is still complex: $\tilde{\varepsilon}_{xx}(\omega) = \varepsilon_1^{xx}(\omega) + i\varepsilon_2^{xx}(\omega)$. Isotropic symmetry makes the xx notation redundant, so we refer instead, to the complex dielectric scalar function, $\varepsilon(\omega) = \varepsilon_1(\omega) + i\varepsilon_2(\omega)$. Over relevant portions of the spectrum, the dielectric function is shaped primarily by electronic excitations of the system. Some of these interactions can be well described within classical models such as those of Drude or Lorentz [34], but the true behaviour is inherently quantum.

Semiconductors in particular differ from other materials in that there are few free electrons at non-zero temperature. The presence of the energy gap separation, E_g, between

26

the electronic conduction and valence states restricts the occupation of the conduction states. In dark conditions (where there are very few/no photons), the only free electrons (or holes) present in the conduction band are those generated by thermal activation or associated with dopants[1]. If a photon has an energy $\hbar\omega$ that is less than E_g (i.e., $\hbar\omega < E_g$), then that photon may propagate without interacting with the electrons. Barring interactions with the lattice, the semiconductor is transparent to light of that wavelength. Conversely, if an incident photon equals or exceeds the gap energy (i.e., $\hbar\omega \geq E_g$) then it is subsequently consumed by interband transitions or other absorbent processes.

The absorption of light is described by the imaginary part of the dielectric function, $\Im\{\varepsilon(\omega)\} = \varepsilon_2(\omega)$. The higher $\varepsilon_2(\omega)$ is, the more likely is the absorption of a photon with frequency $\hbar\omega$. So what factors determine likelihood of a given transition? This question is most often treated within a first order time-dependent perturbation approach from which Fermi's so called *golden rule* is derived. This rule governs the probability and rate of transition of electrons in a solid with unperturbed Hamiltonian H_0 under the imposition of the undulatory Hamiltonian of the electromagnetic field $H'(t)$ so that $H = H_0 + H'(t)$. The generation rate Γ, (which is proportional to the probability of transition) between the valence state $|v\rangle$ and eligible conduction states $|c\rangle$ is

$$\Gamma(\omega) = \frac{2\pi}{\hbar} \sum_c \langle v|H'(t)|c\rangle \langle c|H'(t)|v\rangle \; \delta(E_f - E_i - \hbar\omega).$$

Here, energy is conserved by the Dirac-δ ensuring that the generation rate is non-zero if and only if the energy of the photon $\hbar\omega$ precisely equals the difference in eigenenergies $E_f - E_i$, which is a main deciding factor for the transition. The likelihood of a transition is also related to the overlap element $\langle\psi_f|H'(t)|\psi_i\rangle$. The reverse element $\langle\psi_i|H'(t)|\psi_f\rangle$ is included to account for stimulated emission, i.e., electrons in $|\psi_f\rangle$ which are perturbed by the radiation, causing them to fall to $|\psi_i\rangle$. The rate of generation is an equilibrium between excitations and stimulated emissions. And since $\langle v|H'(t)|c\rangle = \langle c|H'(t)|v\rangle$,

$$\Gamma(\omega) = \frac{2\pi}{\hbar} \sum_c |\langle c|H'(t)|v\rangle|^2 \; \delta(E_f - E_i - \hbar\omega).$$

The elements of the imaginary dielectric tensor can be related to Γ by way of the power loss $\wp = \hbar\omega\Gamma(\omega)$ (for a formal treatment, see Ref. 33). When the wave-functions are expanded as Bloch waves and we consider integration over the first BZ, the diagonal elements of the tensor within the random phase approximation (RPA) [33] (where we renew

---

[1]However, at low temperatures, even electrons associated with dopants can be quenched from the conduction states.
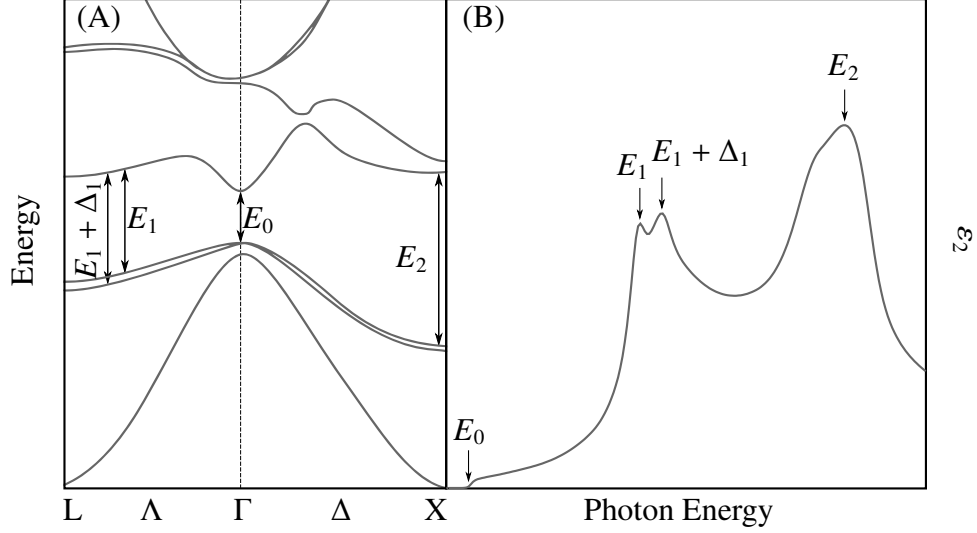
Figure 2.2: An illustration of the relationship between the optical transitions in the electron band structure and their manifestation in the imaginary part of the complex dielectric function. Panel (A), the electron bands for ideal GaAs along paths Λ and Δ with the optical transitions, E_0, E_1, $E_1 + \Delta_1$ and E_2 explicitly marked. These transitions are primary features of the imaginary part of the complex dielectric function and are marked correspondingly in Panel (B), a plot of the imaginary part of the dielectric function of GaAs, experimentally measured [35] at a temperature of approximately 300 K. Panel (A) band data from Ref. 33, Panel B data from Ref. 35

the *xx* superscript notation from earlier) are

$$\varepsilon_2^{xx}(\omega) = \frac{\hbar^2 e^2}{\pi m_e^2 \omega^2} \sum_{vc} \int_{\mathbf{k}} d\mathbf{k}' \ \left| \langle c, \mathbf{k}' | \mathbf{p}^i | v, \mathbf{k}' \rangle \right|^2 \ \delta \left(E_c(\mathbf{k}') - E_v(\mathbf{k}') - \hbar\omega \right). \qquad (2.1)$$

Here, the matrix elements of the momentum operator $\mathbf{p}$ ensure that transition intensities are scaled by the corresponding change in momentum. This enforces selection rules, such as disallowing transitions in which angular momentum is not changed. However, since photons carry insignificant momenta, transitions cannot take place if the total momentum of one wave-function is different from the next. Otherwise, momentum is not conserved. This means that all optical transitions map vertically in energy–momentum space and transitions between $\mathbf{k}$-points are not possible.

The imaginary part of the dielectric function is calculated from Eq. (2.1). In GaAs, there are four main critical points related to landmark interband transitions which are well defined within the band structure and the lineshape of ε_2. These interband transitions and corresponding critical points in the ε_2 lineshape are illustrated in Figure 2.2. The onset of absorption, marked E_0, corresponds to the gap energy at Γ in the centre of the BZ. The set of transitions between the top of the valence band and the bottom of the conduction band

28

consistently spaced in energy along Λ (in the [111] direction of the BZ) manifests itself as the E_1 peak. The top of the valence band is split between Γ and X by an energy Δ_1. This is due to the non-degeneracy of spin-up and spin-down states. These states become split in energy due to the interaction of the spin S with the angular momentum L associated with the wave-function's orbital character about the atomic centre. The so called spin-orbit (SO) coupling is intuitively (but classically) understood in terms of the magnetic fields associated with the 'spinning' electron and the orbital path of the electron. The particle must have more energy if its spin polarity is aligned with its orbital polarity due to the interaction of the magnetic fields. Finally, the E_2 peak, which is a manifestation of transitions along Δ (in the [010] direction of the BZ), similarly comes from a region of the BZ where the top of the valence band and bottom of the conduction band are nearly parallel. There is also some minor splitting along the top of the conduction band, but compared to the E_1 peak, the splitting is smaller; so much so that the individual features are not resolved in ε_2 and one large peak is formed.

2.1.2 Thermal Effects on Band Structure and Optical Properties

The symmetry of an ideal infinite lattice forces the degeneracy of some electron states. Hence, the complex dielectric function of the ideal lattice is distinguished by very sharp features (Figure 2.3), which are not observed experimentally. The presence of thermal perturbations within the lattice breaks the symmetry causing the degenerate states to split. These relationships can be understood in a very intuitive way.

We know that a given wave-function is unique to the potential in which it exists. Let us consider for a moment, the wave-function of an electron with some momentum $\mathbf{k}_1$ in an infinite ideal lattice of P-fold symmetry. The rotational symmetry requires the wave-functions at $P - 1$ other wave-vectors, $\mathbf{k}_2, \ldots, \mathbf{k}_P$, to have the same energy. Why? Because if an observer were to look into those directions, they would see nothing to distinguish one direction from the others, so the potential is therefore not unique; even if the wave-functions are unique to their potentials.

Now, if one of the nuclei in the lattice becomes displaced, it moves nearer to some nuclei and farther to others. An observer in the crystal now has a landmark with which they can distinguish one direction from the rest, and as a result, the symmetry and degeneracy are broken.

To understand more specifically the physical mechanisms which lead to band splitting, let us look at this from a slightly different perspective. We revisit the lattice in which one of
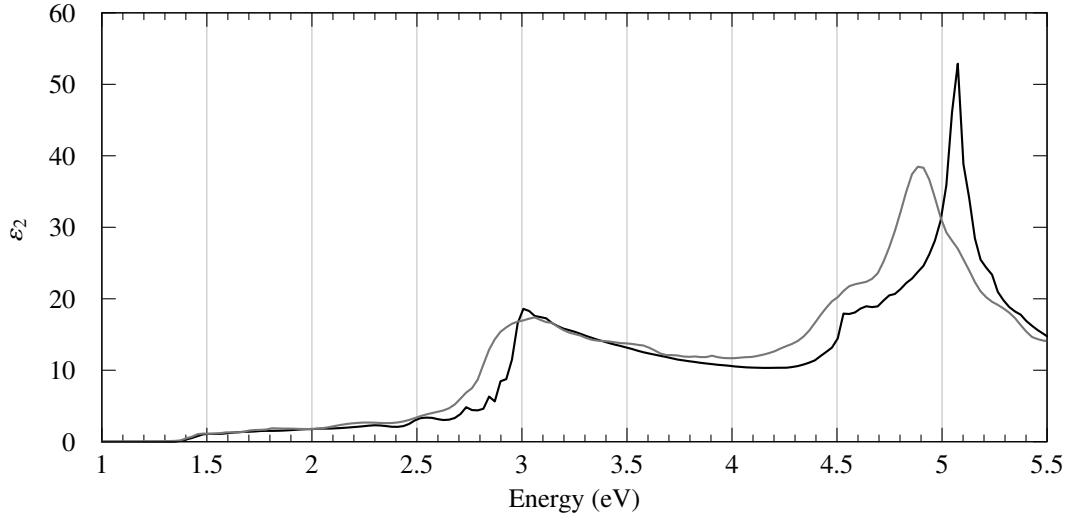
Figure 2.3: Calculated ε_2 for GaAs with ideal lattice positions (black line) and thermal perturbations corresponding to zero-point motion (grey line). Both calculations were non-spin orbital produced in the manner described in §2.2.

the nuclei is displaced. In the regions where the distance between atoms has been closed, the magnitude of the electric field cast by the nuclei is increased, thus deepening the potential for the electrons in that region. Conversely, in the regions where the distance between nuclei has increased, the electric field from the nuclei is diminished, so electrons feel less pull to that region. This situation immediately breaks some degeneracy by offering lower energies to states which concentrate their electrons in the regions between the closely spaced nuclei by splitting previously degenerate states into higher and lower energies. This splitting of states due to thermal displacement is illustrated in Figure 2.4.

Lattice vibrations modulate the overlap of the electronic wave-functions between neighbouring atoms influencing the widths of the energy bands, the energies of interband transitions, and as a result, the optical response. As the temperature increases—resulting in larger nuclear displacements—these effects become intensified. In the static case of perturbed but motionless nuclei, if we consider a valence energy state from which an electron can be excited to either of two split states in the conduction band, one could see that the intensity of the transition would too be split from the united value of the ideal case. The cumulative effect of this splitting over many states in a thermally perturbed lattice is the broadening of the sharp features of ε_2, illustrated in Figure 2.3 which contrasts the imaginary parts of the dielectric functions of an ideal GaAs lattice, and one that is thermally perturbed by
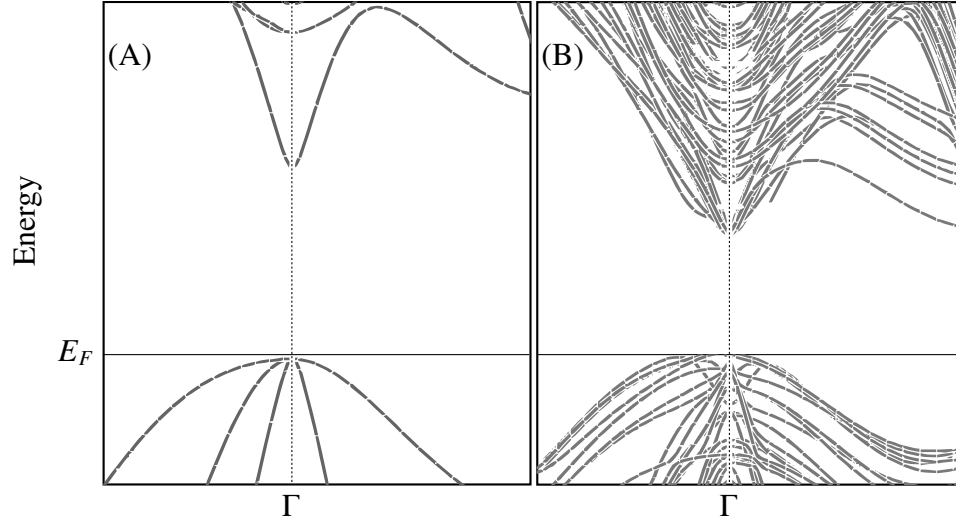
Figure 2.4: Plots of the electron bands in energy-momentum space in the region of the BZ in the neighbourhood of the Γ-point with the energy of the HOMO marked as the Fermi energy E_F. In panel (A), the electrons surround an ideal lattice so electron states are degenerate while in panel (B) the lattice is thermally perturbed such that the temperature corresponds to approximately 1 118 K. The figure demonstrates how symmetry reduction of the lattice breaks the degeneracy of the electron states and reduces the gap energy.

zero-point vibrations.

From a methodological point of view, this broadening could be applied artificially to the complex dielectric function calculated from ideal lattices. Indeed, this has been the only method available to obtain results for ε_2 within experimental agreement. But this sort of data manipulation without a clear physical motivation is not only unsatisfying, it lacks any sort of predictive power. For example, the reduction of the transition energies (redshift) of the E_0, E_1 and E_2 peaks with increasing temperature cannot be realized by simple broadening. Clearly, a model which explicitly accounts for the thermal disordering of the lattice is required to truly understand the linear optical response.

2.1.3 Thermal Expansion

As the temperature of the lattice increases, so does the amplitude of atomic displacements. In harmonic potentials[2], the average displacement of the atoms average simply to the ideal lattice sites and the volume of the unit cell remains constant. More to the point, the average distance between atoms is independent of temperature, so the cell boundaries remain

---

[2]Real atomistic potentials are not harmonic, but at low temperatures, it is often a good approximation.
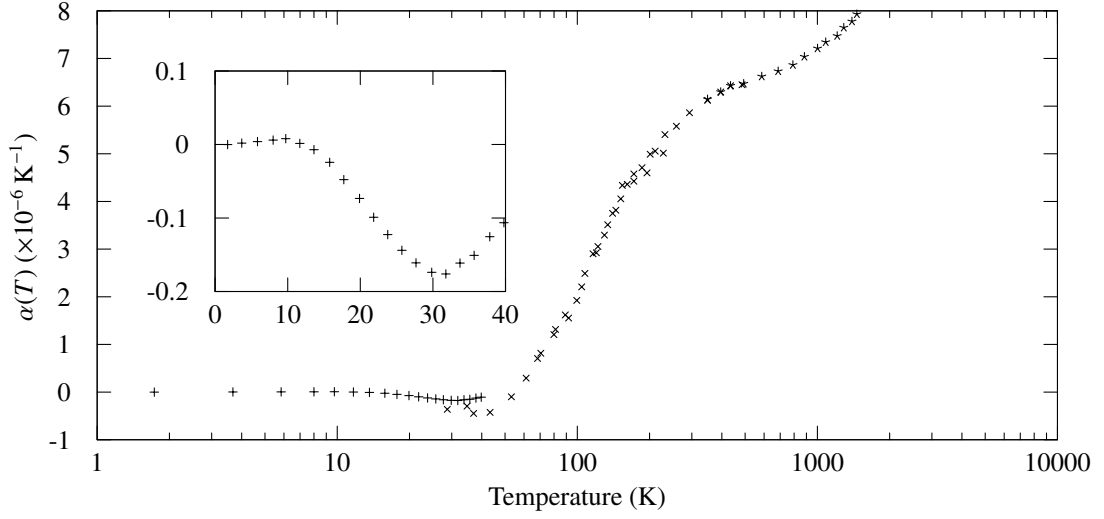
Figure 2.5: A plot of the experimentally obtained thermal expansion coefficient from Ref. 36. The three different point types mark separate experiments across different temperature ranges. The inset plot is simply the lower range data on a non-logarithmic axis for clarity.

constant. The anharmonicity of the true potential energy surface leads to thermal expansion of the cell. As the lattice gains energy, the bonds soften and become longer and the cell expands accordingly. When this happens, the valence states move closer in energy to the conduction states since the expanded bonds are less stable and do not bind the electrons as tightly. So, it takes less energy to excite an electron from the valence band to the conduction band. This all results in a redshift of the complex part of the dielectric function, making thermal expansion a necessary part of the model.

The supercell used during MD calculations had no degree of freedom associated with the cell volume. Since thermal expansion is excluded from the MD portion of our model, it is empirically integrated into our optical formalism. The thermal expansion coefficient α is found experimentally as a function of lattice temperature [36] (see Figure 2.5). The thermal expansion coefficient, defined as,

$$\alpha(T) = \frac{1}{V(T)} \left. \frac{\partial V(T')}{\partial T'} \right|_{T'=T}$$

is integrated to yield a functional equation for the lattice parameter $a[T]$:

$$a[T] = a_{T_0} \left(1 + \int_{T_0}^{T} dT' \, \alpha(T') \right), \tag{2.2}$$

32

where a_{T_0} is some known lattice parameter corresponding to temperature T_0. Equation (2.2) was used to determine the lattice parameter used to define the cell for calculations of optical response and electronic structure after MD.

2.1.4   Experimental Temperature from Mean-Square Displacement

The temperature in molecular dynamics simulations is most often calculated from the statistical relationship between temperature T and the kinetic energy:

$$\frac{3}{2} N_{\mathrm{at}} k_B T = \frac{1}{2} \sum_i m_i \mathbf{v}_i^2, \tag{2.3}$$

where k_B is the Boltzmann constant. While this expression is quite useful, it is only valid for an ideal gas [37]. Furthermore, the effect of using a small supercell, as in the present calculation, is to displace the phonon modes toward the BZ boundary. As a result, fewer phonon modes are excited in the supercell than in the real crystal, so the MD calculation of the kinetic energies of the atoms overestimates the temperature of the configuration.

In order to map the molecular dynamic temperature calculated from Eq. (2.3) to the empirical temperature, we parametrize the mean-square displacement (per atom) $\langle u^2 \rangle$. In the harmonic approximation, we determined the relationship between $\langle u^2 \rangle$ and T from the phonon density of states of bulk GaAs calculated by Giannozzi $et\ al.$ [38],

$$\langle u^2 \rangle = \frac{\hbar^2}{M} \int dE\ \frac{D(E)[n(E,T) + 0.5]}{E}, \tag{2.4}$$

where M is the mass of the primitive unit cell containing one each of Ga and As atoms, E is the phonon energy, and $D(E)$ is the phonon density of states normalized to one primitive unit cell. The occupation of the phonon modes is given by the Bose-Einstein distribution function $n(E,T) = [\exp(E/(k_B T)) - 1]^{-1}$. The term of 0.5 in Eq. (2.4) is a quantum statistical term which accounts for the zero-point vibrations of the lattice. In Figure 2.6, $\langle u^2 \rangle$ for GaAs calculated from Eq. (2.4) in the range from 0 to $1\,100\,\mathrm{K}$ is compared with the results of x-ray diffraction measurements in the range from 85 to $1\,100\,\mathrm{K}$ (Ref. 39, original data from Ref. 40). The calculated $\langle u^2 \rangle$ at absolute-zero temperature is non-zero. This is due to the quantum mechanical effect of zero-point motion of the lattice. To our knowledge, no experimental values for $\langle u^2 \rangle$ have been reported in the range from 0 to 85 K, where zero-point motion is a dominant contributor. In the range from 85 to 600 K, the calculated $\langle u^2 \rangle$ is in very good agreement with the experimental data. At higher temperatures, the experimental $\langle u^2 \rangle$ is strongly influenced by anharmonic effects. Hence, for GaAs, Eq. (2.4)
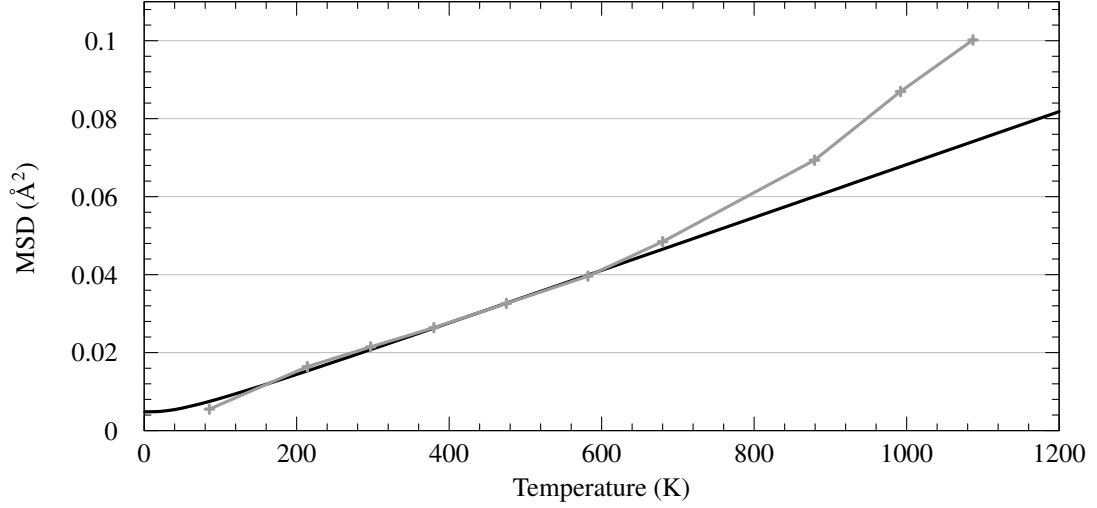
Figure 2.6: (black line) The calculated mean-square displacement $\langle u^2 \rangle$ of GaAs in the harmonic approximation in the temperature range from 0 to 1 100 K, compared with experimental measurements (grey line) in the range from 85 to 1 100 K [39, 40]

is a good approximation only in the temperature range from 0 to about 600 K, where $\langle u^2 \rangle$ is dominated by harmonic effects (phonons), and anharmonic effects can be neglected.

To extract the temperature of each configuration from $\langle u^2 \rangle$ the calculated curve in Figure 2.6 was used in the range from 0 to 600 K, while the experimental curve was used above 600 K.

2.2 Theoretical Methodology

The physical mechanisms responsible for the temperature dependence of the optical properties of semiconductors are traditionally separated into lattice dynamics in the harmonic approximation (i.e., phonons) and anharmonic effects including thermal expansion [41]. The qualitative implications of these mechanisms have been discussed in the preceding sections. This section will proceed as to detail the methodological approach to obtaining quantitative relationships.

In our previous work (Ref. 32), the dielectric function of bulk GaAs was calculated by averaging the optical properties of eight configurations of an 8-atom supercell perturbed by lattice vibrations, following the ergodic hypothesis. For the calculations presented here, a single sixty-four atom supercell (shown in Figure 2.7 in ideal configuration) was used for each calculation of the dielectric function at each temperature. The use of a single larger cell
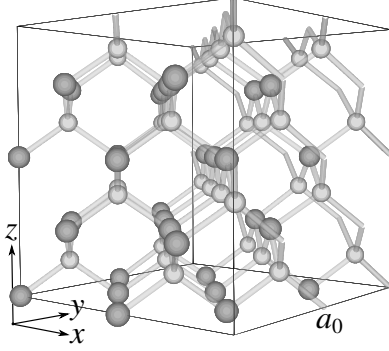
Figure 2.7: The sixty-four (64) atom cubic unit cell of gallium (dark spheres) and arsenic (lighter spheres) shown here in ideal configuration.

precludes the requirement of ergodicity but increases the numerical cost of the calculations considerably.

The representative configurations were extracted from first-principles MD simulations performed with the CP scheme as implemented in the Quantum ESPRESSO software package [42]. For the MD simulations, wave-functions were expanded on a plane-wave basis with an energy cut-off of 12 Ry. Core-valence interaction was described by norm conserving non-local PPs [43, 44] with s and p non-locality. The equilibrium volume of the ideal supercell was determined by minimizing the total energy in the zinc-blende structure, resulting in a cell dimension of 20.44 a.u. Thermal motion of the atoms was achieved by randomly displacing the atoms from their equilibrium lattice positions and then allowing them to move under the action of the atomic forces. Randomization amplitudes varied between 0.61 a.u. and 1.00 a.u. which produce MD temperatures of 509 K and 1 362 K respectively. With one possible exception (discussed later), we found that 35 000 steps, each of 5.0 atomic units of time (1 a.u. = $\hbar/1$ Ht $\approx 2.418\,8 \times 10^{-17}$ s), were sufficient to equilibrate the system, and we extracted the representative configurations over the following 5 000 steps.

Configurations deemed eligible for sampling of optical properties were those in the trajectories which had a mean-square displacement (MSD) within ±3% of the average MSD taken over the final 5 000 time-steps of the run. The eligible configurations were then ranked according to temperature. Those closest (within 5 or 10 K) to the average temperature taken over the final 5 000 time-steps were considered in the final decision. Of the remaining configurations, one was chosen at random to avoid unwanted bias, and then sampled for optics.

The software package WIEN2k [45] was used to calculate the electronic structure and the optical properties of each selected configuration self-consistently using DFT on a APW+lo basis set. Exchange and correlation were treated within the generalized-gradient approximation of PBE [46]. The dielectric function of each selected configuration was

35

calculated in the independent-particle random-phase approximation (RPA) as implemented in the WIEN2k linear optics package, described briefly in §2.1.1. The integral over the wave-vector **k** is evaluated over the first Brillouin zone (Figure 2.1). In evaluating Eq. (2.1), a small but insignificant Lorentzian broadening was applied by the WIEN2k software to smooth out fine grained numerical noise.

It is known that DFT underestimates the energies of the conduction states and hence the energy gaps in semiconductors. To a good approximation, the energies of the conduction states can be corrected by applying the so called scissors operator shift [46] to the eigenvalues independently of **k**-vector. In the present calculations, the DOS and the dielectric functions of all configurations were corrected by applying a scissors shift of 0.80 eV.

Because the thermal perturbations reduce the symmetry of the lattice, a large number of **k**-vectors are required to sample the BZ. For the self-consistent calculations, 172 irreducible **k**-vectors were used, and 868 irreducible **k**-vectors were used to calculate the optical matrix elements. To allow for thermal expansion, the experimentally observed temperature dependence of the lattice constant of bulk GaAs was taken into account as described in §2.1.4. To ensure that the mesh for optics was of sufficient granularity, several calculations were run on coarser and finer grids showing the expected convergent behaviour (§1.3.1). Figure 2.8 shows these calculations, from which it appears that the mesh used for our production calculations was sufficient.

2.3   Results and Discussion

The results of this research are naturally divided into two parts, (1) molecular dynamics and (2) optics. The sections which follow individually describe these two aspects of the research.

2.3.1   Molecular dynamics

Several MD simulations were run in order to obtain trajectories for the sampling of optics. A tabulation of the runs with their respective temperatures is shown in Table 2.1. The MD temperatures were calculated according to Eq. (2.3), and averaged over the final 5 000 steps of the run. The empirical temperature was found graphically by the method outlined in §2.1.4. The reader may notice that the MD temperature of run 0901-1216-24 is higher than that of 0809-2312-14, despite having a smaller MSD and corresponding empirical temperature. This is because a BOMD scheme was used for 0901-1216-24 to better accommodate the low
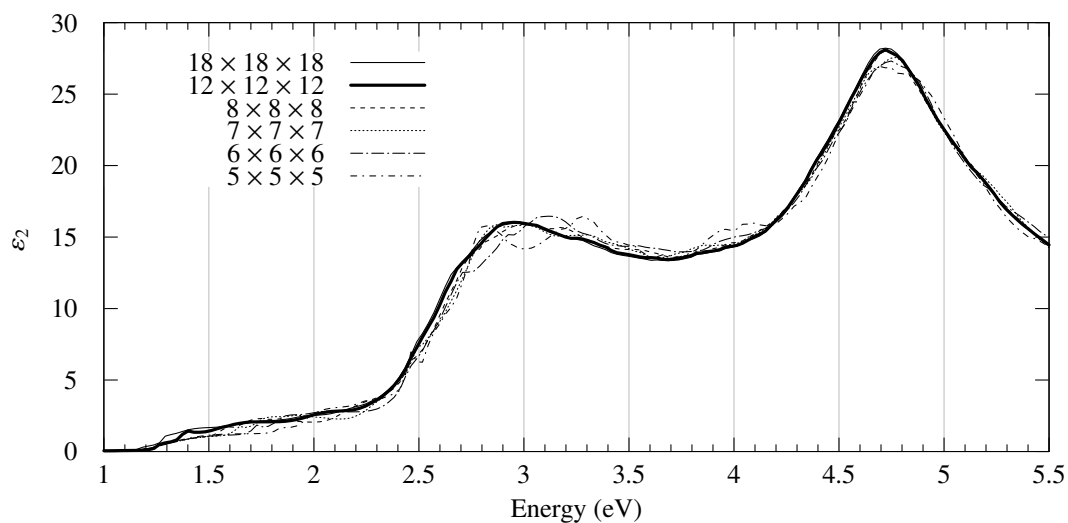
Figure 2.8: A comparison of optical calculations performed on **k**-meshes of various granularity (dashed dotted and otherwise broken lines). The calculation on the **k**-mesh used for production runs is shown (thick black line) to be near the convergent limit. All curves shown here were calculated based on identical potential fields (i.e., were forked from the same SCF calculation).

Table 2.1: A tabular summary relating run ID numbers to corresponding MD Temperature, MSD and empirical temperature.

Run ID	MD Temp. (K)	MSD (Å^2)	Emp. Temp. (K)
0901-1216-24	 126	0.00465	 0
0809-2312-14	 97	0.01272	 160
0809-2312-12	 439	0.02713	 400
0806-1010-56	 509	0.02764	 407
0809-1715-57	 910	0.04469	 635
0807-0201-33	. . . . 1 362	0.07777	 937

37
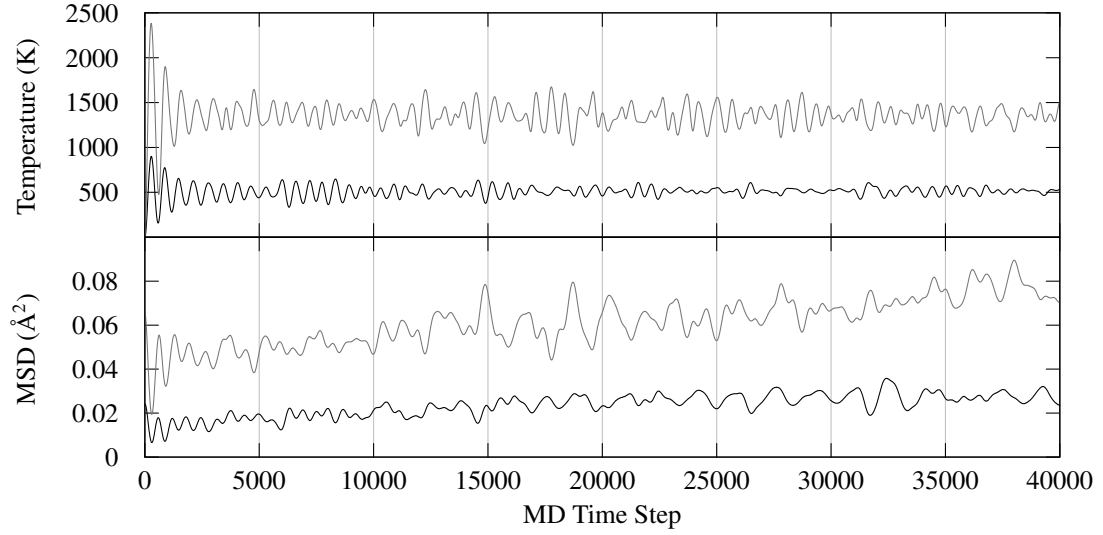
Figure 2.9: Temperature and MSD for runs 0806-1010-56 (black line) and 0807-0201-33 (grey line) over the 40 000 time step duration of the MD simulations.

temperature. The two types of dynamics give slightly different potential energy surfaces, therefore changing the relationship between temperature and MSD.

The evolution of temperature and MSD through two trajectories (0806-1010-56 and 0807-0201-33) are compared in Figure 2.9. The MSD and temperature in Figure 2.9 oscillate due to motion correlation associated with a finite cell, but it is still clear that the MSD of both runs increase with time as the phonon modes of the system saturate to their respective equilibrium populations and the systems thermalize. The accompanying Figure 2.10 demonstrates that different MD calculations at the same temperature can be produced from differing random initial configurations. The second MD trajectory in this figure is 60 000 time steps longer than 0807-0201-33, allowing us to gauge the time-scales of the thermalization processes. It might be argued that the 0807-0201-33 trajectory could benefit from slightly longer thermalization time, which could be taken into account for future calculations.

2.3.2 Optics

Continuing our procedure from the MD of 0806-1010-56 and 0807-0201-33, representative configurations (chosen as described in the last section) were extracted from each of the trajectories. Optical calculations were performed and compared to results from Ref. 32

38
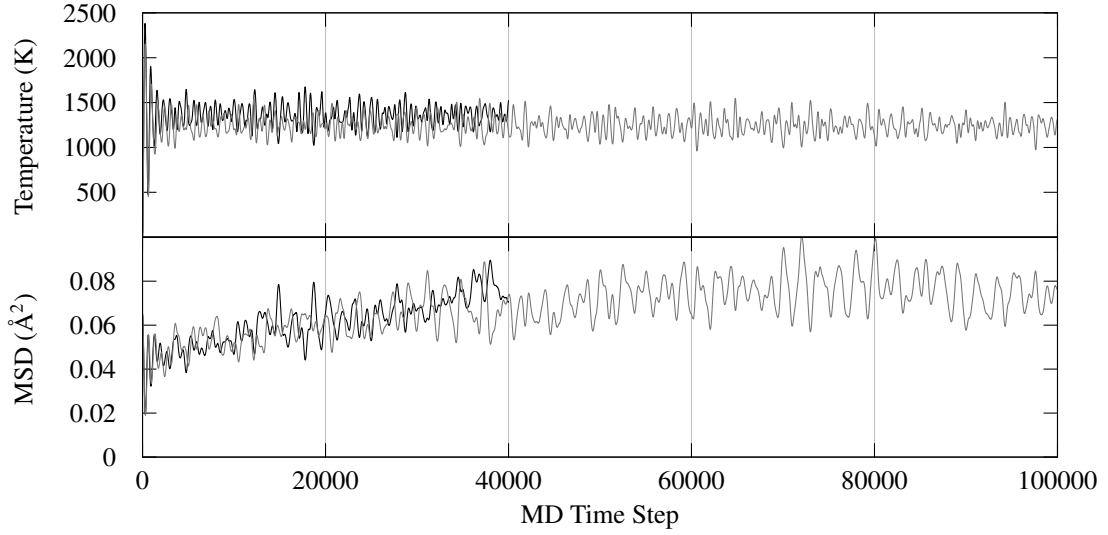
Figure 2.10: A plot of temperature and MSD of 0807-0201-33 and the extended 100 000 time step simulations showing that the tail end of the 0807-0201-33 simulation has reached a reasonable (if not complete) thermal equilibrium.

(Figure 2.11) and experimental data from Ref. 35 (Figure 2.12). Figure 2.11 shows compatibility between the method used in Ref. 32 and the somewhat more refined method used for the present calculations. There are noticeable quantitative differences in the positioning and the overall shape of the curves. To clarify the origin of these differences, a single calculation from Ref. 32 was repeated within the software environment used in the present calculations, and the results were compared to the original data from Ref. 32. From that comparison, it was apparent to us that the newer software environment yields quantitatively different results which can be mainly summarized as a slight redshift of approximately 0.16 eV. This accounts for some difference in peak position. The differences which remain, including the qualitative differences in lineshape, are effects due to the larger cell considered by the present calculations.

The computed imaginary parts of the dielectric functions from all sampled temperatures are plotted in Figure 2.13, with experimental data and data obtained from the 8-atom calculations for comparison. In this figure, we see the effects of temperature broadening the sharp features and redshift of the E_1 and E_2 peaks in all three data sets. The onset of optical absorption, E_0 is also redshifted as the temperature increases. We know that the onset of absorption is due to transitions across the band gap near Γ in the centre of the BZ.

39
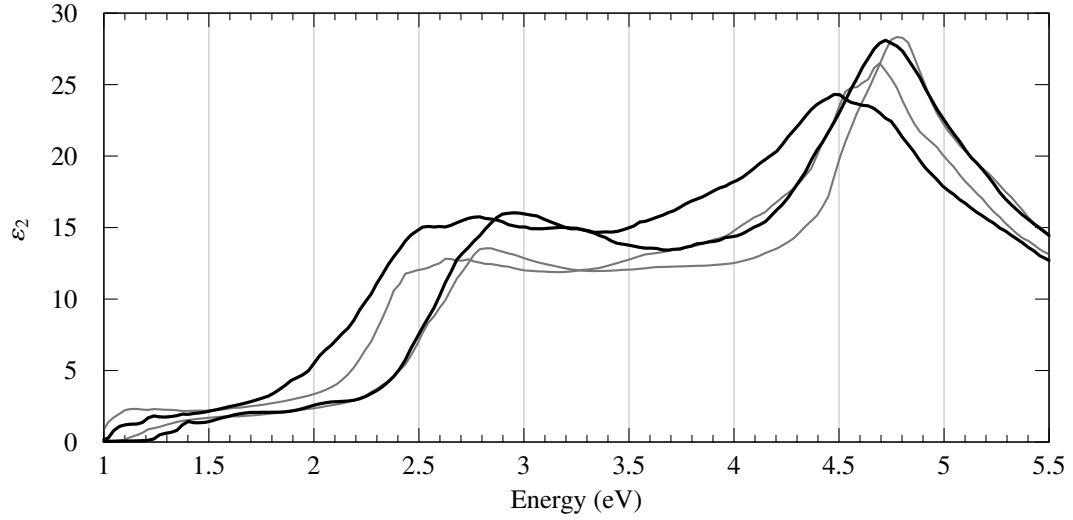
Figure 2.11: The imaginary dielectric functions for 0806-1010-56 and 0807-0201-33 (thick black lines) plotted against those calculated from eight atom cells in Ref. 32 (fine grey lines) at 315 K and 705 K. The higher temperature lines in each case are distinguished as lower and broader.
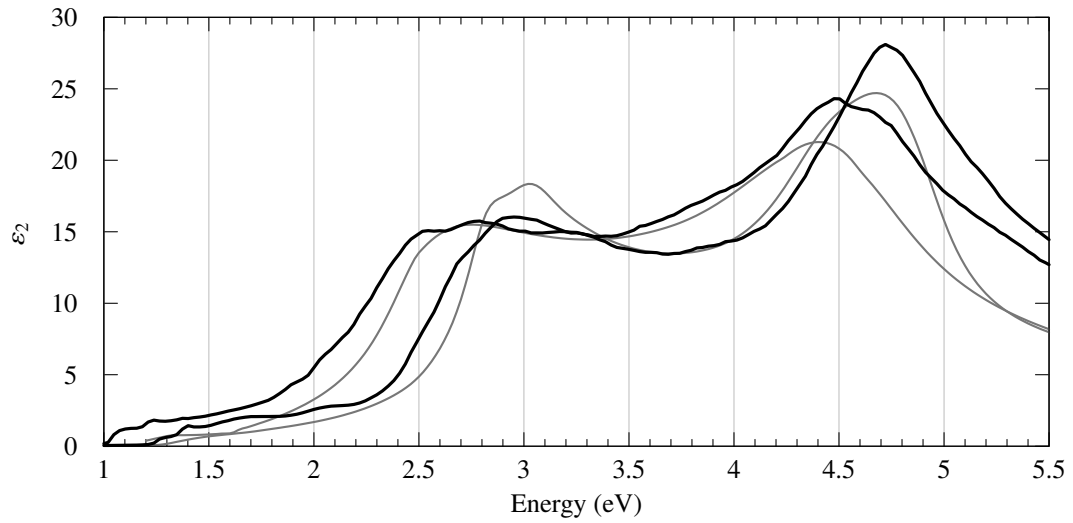
Figure 2.12: The imaginary dielectric functions for 0806-1010-56 and 0807-0201-33 (thick black lines) plotted against the experimentally measured data from Ref. 35 (fine grey lines), for temperatures of 473 K and 1 073 K. The higher temperature lines in each case are distinguished as lower and broader.
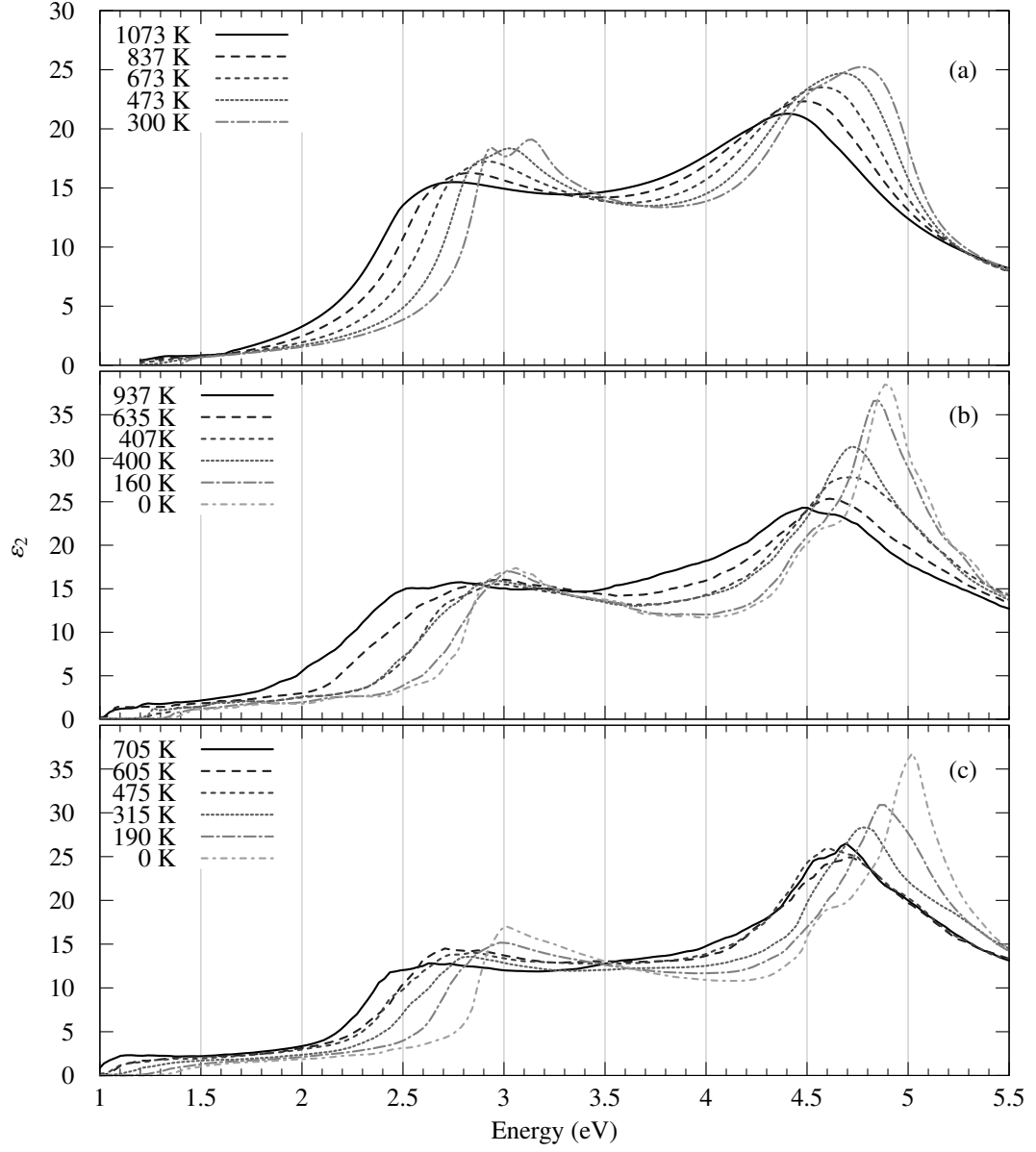
Figure 2.13: A plot of the temperature dependence of the imaginary part of the dielectric function for GaAs based on (a) experimental data from Ref. 35, (b) the present calculations with a 64-atom unit cell corresponding to the MD simulations in Table 2.1 and (c) previous calculations in Ref. 32.
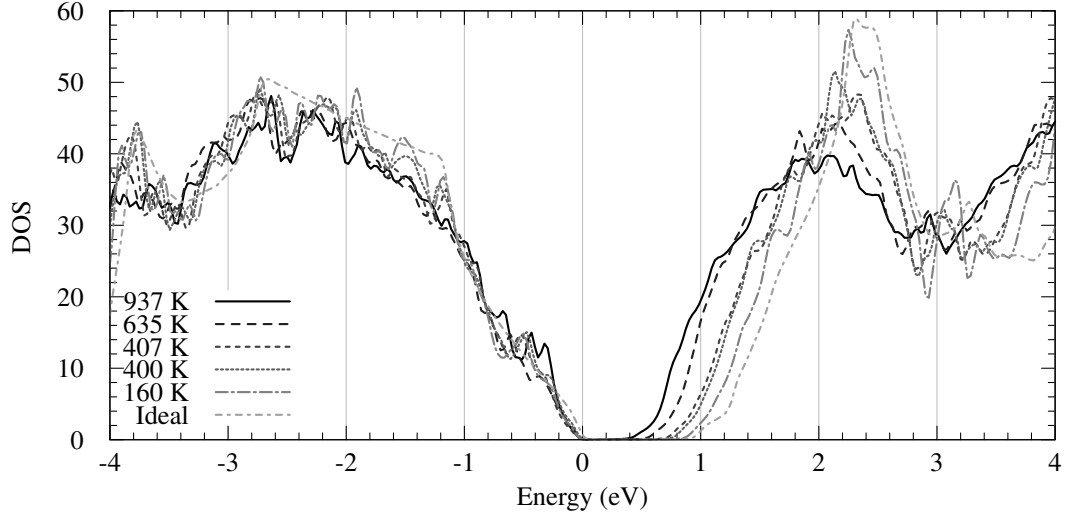
Figure 2.14: A summary plot of the density of states for GaAs based on a 64-atom unit cell with thermal perturbations in the temperature range from 0 K to 1 362 K corresponding to the MD simulations in Table 2.1.

This gap is precisely manifested as a zero density gap in the DOS, shown in Figure 2.14 for the calculations on the 64-atom unit cell. In that figure, we see the gap eroded as the temperature increases, making the absorption onset a decreasing function of temperature. From the data, we can conclude that the gaps along Λ and Δ responsible for the E_1 and E_2 peaks (Figure 2.2) are also reduced by increasing temperature—resulting in the overall redshift of those peaks as well.

As stated earlier, the effects of temperature on optics are often divided between harmonic and anharmonic contributions, thermal expansion being an anharmonic one. We have previously demonstrated that thermal expansion causes a slight redshift in the overall spectrum which results from the expanding and weakened bonds (§2.1.3). We have found that this effect is small compared to the other harmonic effects and can therefore state that the closing of the $\mathbf{k}$-dependent gaps between conduction and valence states comes primarily from the perturbation of the lattice and not thermal expansion.

In Figure 2.15 we show the critical point energies obtained from our lineshape analysis of the calculated ε_2 curves. It is compared there with experimental data from Refs. 35 and 47. For the E_2 peaks, we see good agreement with both sets of experimental data in terms of slope. Although our data contains SO contribution and therefore has no $E_1 + \Delta_1$ points, we consider good agreement for E_1 to be anywhere between the experimentally measured E_1 and $E_1 + \Delta_1$ points. Under that criterion, we also see good agreement of the E_1

Figure 2.15: Temperature dependence of the main critical point energies of the imaginary part of the dielectric function of GaAs. The data from the present calculations are marked with crosses (×) and connected with lines for clarity, experimental data from Trepk in Ref. 35 are marked with hollow squares (□), and experimental data from Lautenschlager *et al.* in Ref 47 are marked with downward pointing hollow triangles (▽).

peaks with experimental data.

It should be noted here that our formalism can include the SO contributions required to form the separate E_1 and $E_1 + \Delta_1$ peaks, but this unnecessarily adds a significant computational cost. We have successfully run such calculations as tests using 8-atom cells with favourable results.

Continuing with the analysis of Figure 2.15, the two highest temperature points from the 64 atom cell appear awkwardly high in comparison to our data at lower temperatures. Looking once again to Figure 2.13, one sees that it is not straightforward to qualitatively determine the energy at which the E_1 peak is located on the ε_2 curve for 937 K. There is no quantitative problem since there is clearly a maxima for that peak, but it does not appear to be naturally placed on the curve. Temperature has broadened the peak into a flat shoulder and it is difficult to see where the peak should be relative to the smaller order peaks that are effects of sampling a finite cell. Here, we are once again seeing the MSD of the atoms becoming too large compared to the size of the cell which is adversely affecting the optical response.

To remove the smaller order peaks which obscure the true curvature of the shoulder, a low-pass fast Fourier transform (FFT) filter was applied. Energy oscillations above $2.25\,\mathrm{eV}^{-1}$
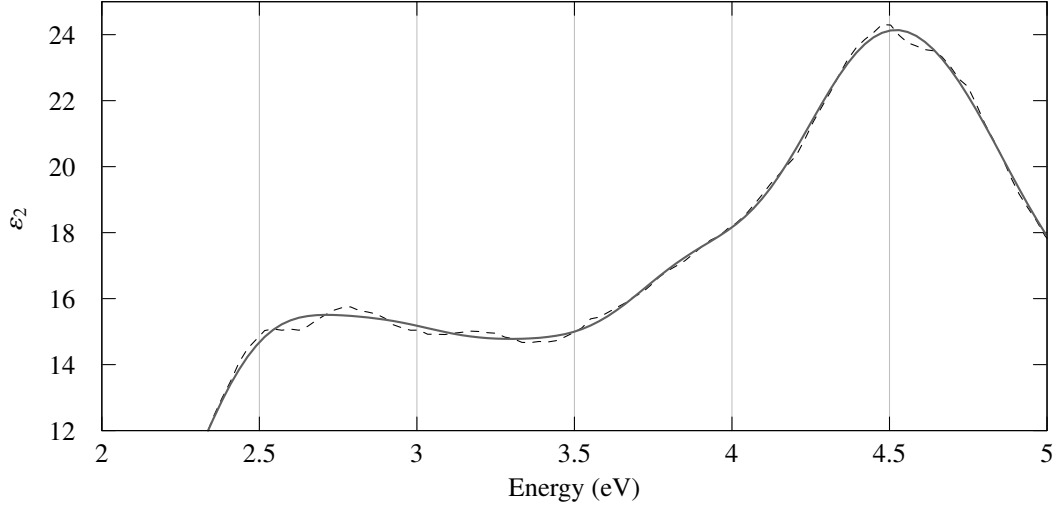
Figure 2.16: A plot of ε_2 for the 937 K data (solid line) and the same data filtered through an FFT low-pass with a cutoff of 2.25 eV^{-1}.

were extinguished, leaving the smooth shoulder to be easily read (Figure 2.16). For the 937 K critical points, there is a clear improvement, but there is essentially no difference for lower temperatures. A plot with the adjusted critical points for 937 K and 635 K is presented in Figure 2.17.

The overall agreement with experiment is astonishing when one recalls the long pathway of approximations that lead to these results. These results affirm the method as the first standard for calculating temperature dependent optical properties within the frozen phonon approximation. Through it, we have gained a fundamental understanding of the nature of broadening and redshift of the complex part of linear optical dielectric function.

2.4   Conclusion

In this chapter we have presented a method of computing the linear optical response of crystalline semiconductors within the framework of widely available DFT implementations. Emphasis was placed on capturing the effects of the thermally perturbed lattice on the adiabatically isolated electronic structure, which has not been done prior to our previous works from Ref. 32, which was a proof of concept based on a case study on an 8-atom cell of GaAs bulk. The present research extended the proof of concept by improving upon the model of the supercell. In particular, the present calculations are modeled upon a larger
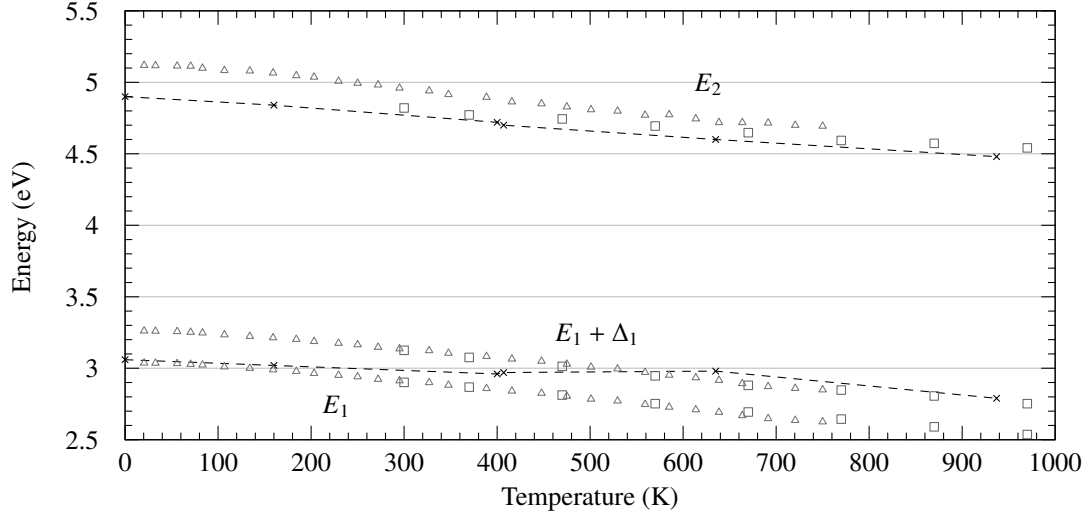
44
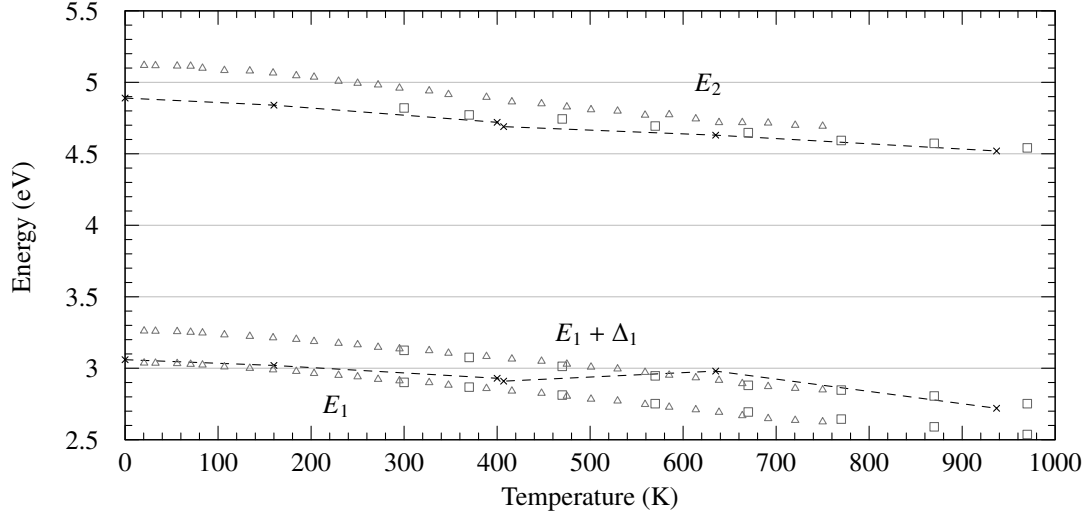
Figure 2.17: Temperature dependence of the main critical point energies of the imaginary part of the dielectric function of GaAs, as in Figure 2.15. The data from the present calculations, this time modified by an FFT low-pass filter, are marked with crosses (×) and connected with lines for clarity, experimental data from Trepk in Ref. 35 are marked with hollow squares (□), and experimental data from Lautenschlager *et al.* in Ref 47 are marked with downward pointing hollow triangles (▽).

64-atom cell of GaAs, which extends the temperature range of our method closer to the melting point of the material.

Several issues arose during the research which show a future direction for the method. Specifically, longer MD simulations should be used to ensure better thermalization of the cell. Also, a unified approach to MD simulations should be taken, where we were forced to change our MD formalism in order to achieve lower temperatures.

Despite these issues, the research presented here is extremely relevant. It represents a major step in the development of a ground breaking method for computing temperature dependent optical properties of crystalline solids. The results obtained from this method are very good at qualitatively and quantitatively predicting the temperature dependence of the imaginary part of the complex linear dielectric function.

C(111) 2×1 Revisited: Surface Band Structure
Modified by Top Layer Dynamics

DIAMOND and related materials have lately received a great deal of attention from the scientific and engineering communities. Nanocrystalline and polycrystalline diamond-like thin films and diamond-like carbon are promising materials for modern technology. Their exceptional mechanical, electrochemical, electronic and optical properties uniquely suits these materials for special applications. For instance, the extreme chemical inertness and biocompatibility of diamond-like thin films has recently found application as a coatings for biomedical implants [48] which greatly reduce or eliminate the risk of rejection. Diamond-like carbon is also well established in electronic hardware applications and has applicability in a range of industries including the medical, aerospace and manufacturing sectors. With both diamond-like and graphitic bonding configurations, this versatile material can be tailored for lubricity, hardness, elasticity, electrical properties, hydrophobicity and alike. A range of applications can be facilitated and improved with specially optimised surfaces.

The C(111) 2×1 reconstruction surface in particular holds many interests, both of practical and academic nature. The (111) face is the cleavage face of diamond and has many specific applications including epitaxial growth substrates, electronic and optoelectronic devices and the biomedical films mentioned earlier. Perhaps its most provocative mark is the controversy which it has held for the past two decades. While similar surfaces for Si and Ge are well understood, to the best of our knowledge, nobody has been able to fully consolidate theory and experiment on the C(111) 2×1 surface. *Ab-initio* calculations [49–53] within the DFT formalism predict the surface to be (semi-)metallic [54, 55] while optical

experiments [56] show the surface to be semiconducting with a gap around 1.47 eV.

It is readily shown that the presence of well defined static symmetry breaking distortions can open the electric band gap [51, 57], but all recent state of the art investigations have concluded that the relaxed reconstructed (111) surface has no such distortions [58].

We show here that the gap at the surface is attributed not only to the many-body effects from excited states but also to electron–phonon interaction. Recent calculations [50, 58, 59] have attempted to confront the problem of many-body effects by extension of the DFT wave-functions. It appears however that under this theoretical methodology, the two mechanisms responsible for the gap cannot be independent of each other. In this chapter, we propose that in order to generate the correct DFT wave-functions with which to predict many-body properties, the dynamical motion of the atoms must first be considered. A starting point is to study the vibrational properties of the surface and the consequential electron–phonon interaction.

The vibrational properties of $C(111) 2 \times 1$ are an important ingredient of the microscopic description of the physical processes at the surface, but there are no recent vibrational investigations of this surface available. It is from this point that we present an in-depth study of the structure and dynamical motion of the $C(111) 2 \times 1$ surface with emphasis on the phonon modes at the surface and their impact on electronic structure. We also look briefly at the possibility of larger order reconstructions such as those found for the well known Si(100) 2×1 reconstruction [60].

3.1   Theoretical Background

The scientific understanding of this surface is constantly changing and still incomplete. The goal of this research is to take our understanding a step farther by examining the dynamics of the top layers and the effect of such dynamics on the electronic structure. In the sections to follow, key concepts will be introduced to build a working basis for interpreting our theoretical findings. Such key concepts include truncated diamond surfaces and the 2×1 reconstruction, surface phonons, surface band structure, electron–phonon interaction and zero-point motion.

3.1.1 Reconstruction, the Pandey surface and the surface Brillouin zone

A surface is first formed when the bulk solid is truncated along some given plane. This requires the division of electronic bonding pairs along the truncating plane—with the remaining (non-truncated) electrons in orbitals *dangling* into the newly formed vacuum. These so called *dangling bonds (DB)* are chemically active sites which increase the total energy of the surface making it unstable with respect to surface structural phase transitions. During these phase transitions, the surface is said to be *reconstructing* itself to lower its energy. Often there is some activation energy for the phase transition, which can be overcome by annealing the surface.

In our case, we consider the surface of diamond truncated along one of the {111} planes. This set of planes can yield two symmetrically inequivalent surfaces. The natural cleavage surface of diamond is the so called *single dangling bond* surface, in which only one bond per primitive cell is broken. This is the surface considered in the present research. The other possibility, the so called *triple dangling bond* surface, does not occur naturally.

The generally accepted model for the reconstruction of the single dangling bond $C(111)$ surface is the 2×1 Pandey model [58]. The reconstructed surface is compared to the truncated bulk surface in Figure 3.1. In the reconstructed surface, the dangling bonds are chemically passivated when the truncated surface folds into π-bonded chain structures parallel to the $[\bar{1}10]$ direction. The formation of the chains modifies the geometry of the hexagonal rings of the truncated surface, seen when looking into the $[\bar{1}10]$ direction. They are reconstructed into alternating heptagon–pentagon rings, reducing the symmetry of the surface.

The '2×1' declaration in the name $C(111)\, 2 \times 1$ is the so called Wood notation. It indicates the ratios of the lengths of the 2D Bravais lattices [34] of the reconstructed surface to the unreconstructed surface. For this chapter, the notation will be extended to describe the number of unit cells which are combined to make a supercell. For example, many of the simulations presented in this chapter were performed on four 2×1 unit cells stacked in a 2-by-2 array. That supercell is hence referred to as a 4×2 supercell and is illustrated in Figure 3.2(a). Larger order reconstructions were investigated with eight 2×1 unit cells stacked in a 2-by-4 array which is thus called a 4×4 supercell.

The surface Brillouin zone (SBZ) for the $C(111)\, 2 \times 1$ surface is illustrated in Figure 3.2(b). The BZs of surfaces are reduced dimensionally, due to the lack of symmetry in the direction perpendicular to the surface. Truncating an infinite crystal creates an infinite
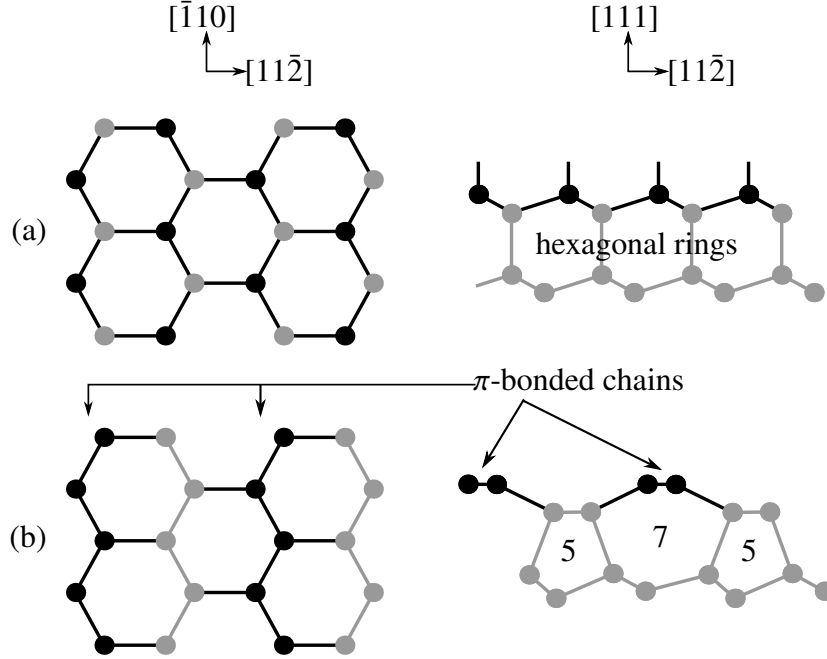
Figure 3.1: Orthographically projected top and side views of the C (111) surface (a) in ideal configuration from truncated bulk and (b) the 2×1 π-bonded chain model of Pandey [58]. Black circles denote first-layer atoms. The π-bonded chains of the reconstructed surface as well as hexagonal, pentagonal and heptagonal ring structures are marked.

vacuum above an infinite bulk. This situation precludes the possibility of translational symmetry in the direction perpendicular to the surface. Hence, the unit cell of a surface must contain at least one infinite lattice vector which reduces the BZ to two dimensions.

3.1.2 Symmetry reduction and the electronic band gap

In principle, a semiconductor surface tends to be insulating or semiconducting [57]. It is well known however that the ideal Pandey surface for the case of C(111) 2×1 within DFT and similar formalisms is semi-metallic [49, 52, 61]. This is in direct conflict with experiments, which show the surface to be semiconducting [56]. Studies have found that certain types of distortion of the π-bonded Pandey chains can open the DFT gap and qualitatively restore the semiconducting property of the surface [51, 57]. These distortions, illustrated in Figure 3.3, reduce the symmetry of the surface by breaking the geometric equivalence of the atoms in the chains.

Chain tilting breaks the equivalence in the [111] direction by raising one side of a chain above the other, resulting in a charge transfer between the raised and lowered atoms. The
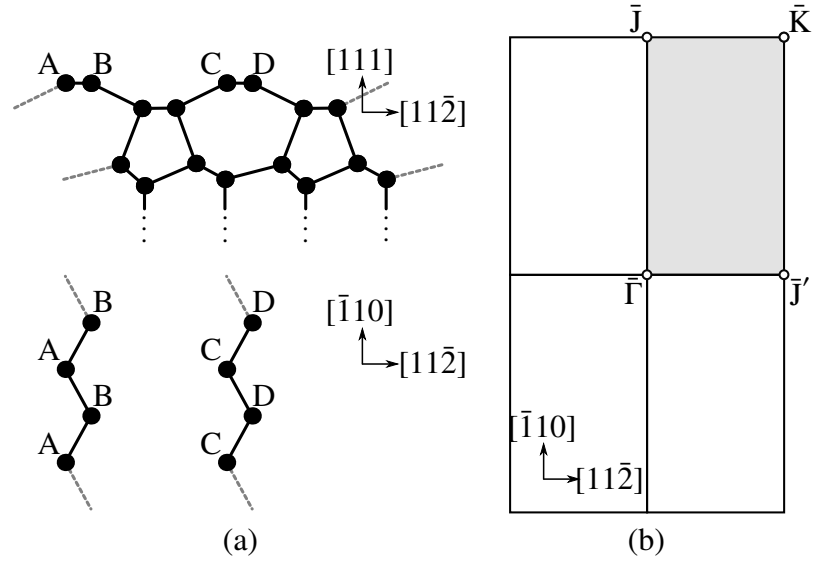
Figure 3.2: (a) Orthographic projection (top) looking along the π-bonded chains into the $[\bar{1}10]$ direction and (bottom) looking downward onto the π-bonded chains. Dashed bonds indicate bonds which extend across the super-cell boundary while solid bonds connect atoms within the super-cell basis. Letters A, B, C and D mark atoms along the sides of the top two chains in the super-cell. (b) The surface Brillouin zone for the C(111) 2×1 cell with high symmetry points marked. The irreducible part of the Brillouin zone is shaded grey.
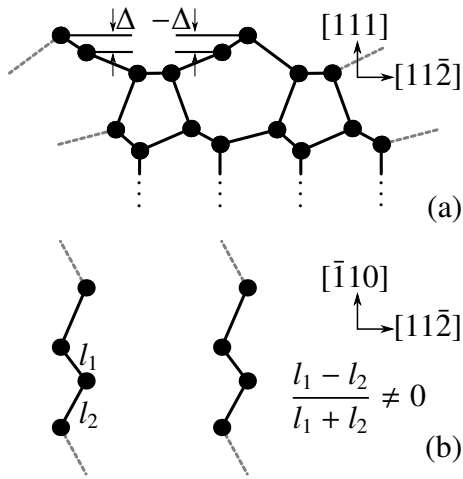
Figure 3.3: This figure demonstrates the two main types of chain distortions, (a) buckling and (b) dimerization.

elevated atoms draw charge from the lower atoms because of the distension or compression of the bonds to layer-two atoms. The bonds between the lowered chain atoms and the layer-two atoms are compressed, increasing the Coulomb interaction between the electrons in the compressed bond and the electrons in the chain bonds. This forces the electrons in the chain bonds toward the raised atoms, which accept the charge more readily because of the distended bonds between the raised atoms and the layer-two atoms. The buckling is quantified by the distance, Δ, that one side of the chain moves above the other. A particular side of the chain is arbitrarily designated as dominant, and so, Δ is positive when the dominant side is raised above the other side, and negative when the dominant side is lowered. In the case where there are thermal perturbations present, the height of the chain, $\langle z_i \rangle$, is taken to be the average height of all of the atoms in the chain, $\{z_i\}$.

In contrast, dimerization breaks the equivalence of the surface atoms in the $[\bar{1}10]$ direction by alternating the bond lengths l_1 and l_2 along the chains. This involves shifting of charges, but does not significantly affect the ionic character of the surface. Dimerization is quantified by the dimerization coefficient $d = (l_1 - l_2)/(l_1 + l_2)$, which is often expressed as a percentage. When thermal perturbations are present, or more than one dimer is present, then d is calculated for each triplet (or zig-zag of the chain,) and the absolute value is averaged. We take the absolute average, $\langle |d| \rangle$, because $\langle d \rangle$ is obscured by the cancellation of positive and negative values.

These distortions of the π-bonded chains open the gap because they allow the delocalized π states to localize near one of the geometrically inequivalent atoms. The physical mechanism linking localization to the opening of the gap is the orthogonality of the wave-functions. The π^* states of the ideal chain are localized in all cases, so orthogonality is easily maintained between the delocalized π and localized π^* states on the ideal Pandey surface. This is true simply by virtue of having the localized and delocalized states occupying different space. Even though some space is shared by the two orbitals, it is energetically of small consequence for the wave-functions to undulate slightly so that their inner product remains zero. When the π states become localized due to dimerization, the π wave-functions are concentrated into the same volume as the π^* wave-functions. The only way for them to maintain orthogonality in this case is for their spatial oscillations to align in such a way that $\langle \pi | \pi^* \rangle = 0$, forcing one of them to be higher in energy than the other. This is the origin of the electronic band-gap.

It is worth noting that the notion of thermal perturbations causing an opening of the gap is contrary to what is expected of any other material. In Chapter 2, we explained in detail why the presence of thermal perturbations reduces band-gaps. For the C(111) 2×1 surface,

the presence of the delocalized–localized transition of the π-state, unique to this surface, is the cause of this contrary behaviour.

3.1.3 The role of dynamical motion in the band-gap problem

While buckling distortions, even at unphysical levels do not significantly affect the surface electronic structure [57], dimerization is found to effectively recover the semiconducting character of the surface [49–52, 59]. The conflict between theory and experiment remains however, since all well converged DFT calculations show that the $C(111)\,2 \times 1$ surface relaxes to the ideal Pandey surface [50, and references therein].

Efforts to resolve this conflict have focused on improving theoretical descriptions of the electronic configuration of the surface [50, 58]. The main failing of DFT in the case of $C(111)\,2 \times 1$ has been postulated to be the inability of DFT to describe excited electronic states. Calculations [50] using a self consistent GW [29–31] approach have shown that the gap between the bonding (π) and anti-bonding (π^*) surface states may be opened by excitations of the electronic structure, but the semi-metallic wave-functions yielded by DFT do not provide a reliable zeroth-order eigenset for GW calculations [58]. The DFT wave-functions are incorrect because the occupation of the π^* orbitals in ground state (due to the lack of a surface gap) causes a miscalculation of the potential. The DFT wave-functions cannot then be extended within a GW framework. It appears paradoxically that in order to obtain a gap from DFT wave-functions, we must start in the first place with a gap.

We propose here, that inclusion of electron-phonon interaction will open the surface gap enough that the DFT wave-functions become viable as a basis for GW calculations. We justify this by pointing out that the existence of Jahn-Teller-like [62] phonon-modes are naturally expected and provide the dimerization required to open the gap at the DFT level. The light nuclei of carbon are highly subject to quantum effects, including zero-point motion, where atoms vibrate to observe the uncertainty principle. The Debye temperature of bulk diamond ranges between $1\,762\,\text{K}$ and $2\,020\,\text{K}$ [63, 64], making diamond a quantum-crystal at room temperature [65]. So, even though the relaxed $C(111)\,2 \times 1$ surface conforms to the ideal Pandey model in the electronic ground state of the classical point potential, it does not occur in nature where the nuclei are in fact highly quantum particles.

Notably, this may not be the only argument for why the ideal Pandey surface may not exist naturally. For instance, we are currently exploring the possibility and consequences of hydrogen impurities. There are many possibilities which might force a break in symmetry, resulting in the localization of surface states and opening the gap. We maintain only that the
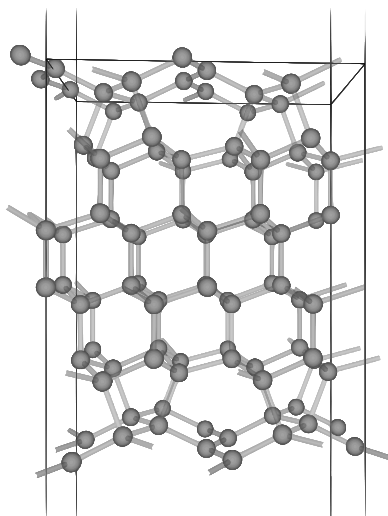
Figure 3.4: A perspective view of the ideal atomic configuration for the $C(111) \, 4 \times 2$ slab supercell used for many of the calculations presented herein. The cell contains 96 atoms across 12 layers. Cell dimensions are listed in Table 3.1

ideal Pandey surface does not correspond to that which is used in experiments.

3.1.4 Higher order reconstruction

As a compliment to this research, we also investigate the possibility of higher order reconstruction of the surface. A larger cell may reconstruct differently than a smaller cell because it has more degrees of freedom. For example, long range interaction between the chains (possibly through the bonding structure of lower layers) may result in a $\{\pm\Delta, \, \mp\Delta, \, \pm\Delta, \, \dots\}$ buckling pattern. Since dimerization is known to affect the gap most, it is of particular importance to determine if any sort of pattern of the π-bond lengths is found over a larger cell.

3.2 Theoretical Methodology

The theoretical methodology is described in five parts. The cells used for *ab-initio* modelling of the surface are described in §3.2.1. The details specific to the studies of ideal geometry (relaxation studies), molecular dynamics, electronic structure and vibrational analysis are presented in §3.2.2, §3.2.3, §3.2.4 and §3.2.5 respectively.

3.2.1 Supercells

Several supercells were modelled to determine various properties of the $C(111) \, 2 \times 1$ surface. The supercell most used was the 4×2 cell illustrated in Figure 3.4. Unless otherwise noted, all generic or ambiguous references to a supercell are referring to the 4×2 supercell. Others

Table 3.1: A summary of the three supercells used, including number of atoms and layers, cell dimensions and slab type. Types are distinguished as either symmetric (S) or hydrogen terminated (HT). The magnitudes of the lattice vectors of the cell, a, b and c correspond to the directions $[11\bar{2}]$, $[\bar{1}10]$ and $[111]$ respectively.

Slab	# of C atoms	# of C layers	a (a.u.)	b/a	c/a	Type
2×1	24	12	8.2060	0.5774	3.9559	S
4×2	96	12	16.5104	0.5774	2.5588	S
4×4	94	6	16.5104	1.1547	1.7646	HT

used for the present research are 2×1 and 4×4 supercells. A tabular summary of these cells and their parameters is shown in Table 3.1. The table distinguishes hydrogen-terminated slabs from symmetric slabs. Symmetric slabs are those in which a plane of symmetry may be inscribed through the center of the slab. Hence, symmetric slabs have two surfaces. This is in contrast to hydrogen-terminated slabs, which have only one clean surface while the other surface is coated with a monolayer of atomic hydrogen. The hydrogen monolayer hinders interaction between the two surfaces, so thinner slabs may be used. This was advantageous for the 4×4 slab, since a thicker slab would have been too computationally expensive.

In all cases, core-valence interaction for carbon atoms was described by a norm-conserving non-local PP [66], with s-only non-locality. In cases where a hydrogen monolayer was used to terminate a slab, the hydrogen core-valence interaction was described by a local PP [67].

3.2.2 Surface relaxation studies

Two different formalisms were used to obtain forces and evolve the non-linear optimization schemes for lattice geometry: CP dynamics, with wave-functions propagated with the CP Lagrangian mechanics, and a scheme reminiscent of BOMD, wherein the electronic degrees are brought self-consistently to ground state each time the ions are moved. Geometry relaxations within the CP formalism employed a simple steepest-decent algorithm to traject the ions while the BO-type relaxations were directed by the more sophisticated Broyden-Fletcher-Goldfarb-Shanno (BFGS) [68–71] algorithm.

For most relaxations, the basis-set cut-off energy was 50 Ry, although 20 Ry was used for one particular case, for the sake of comparison to Ref. 51. Carbon atoms require a relatively high kinetic energy cut-off, since the steep potential undulates the valence wave-functions. The core potential of carbon atoms is steep because the carbon nucleus is poorly shielded by its core $1s$ electrons.

During all relaxations (except those on the 4×4 cell), all atoms were free to move, ensuring that no forces from fixed atom structures influence the minimum energy configuration of the top layers. In the 4×4 cell, the bottom layer of carbon atoms was fixed in place and bonded to a free moving monolayer of atomic hydrogen, and all other atoms were free to move.

3.2.3   Molecular dynamics

Several molecular dynamics simulations were run under both CPMD and BOMD schemes, for each of 4×2 and 4×4 surfaces. The results of the relaxation studies indicated that BOMD would be the best choice for for accuracy of the structure and vibrational properties.

The main production MD simulation, from which vibrational properties were extracted, was performed on the 4 supercell with a cutoff of 50 Ry. The two central layers of the slab were held in fixed positions to decouple the motion of the two sides of the slab. The ionic equations of motion were integrated with a time-step of 15.0 a.u. (with 1 a.u. $= \hbar/1\,\mathrm{Ry} \approx 4.837\,8 \times 10^{-17}\,\mathrm{s}$).

The BZ was sampled by a uniform $3 \times 4 \times 1$ **k**-point grid over the entire SBZ. This mesh represents four non-equivalent points in the irreducible Brillouin zone (IBZ). The motivation for this choice is discussed in the next section.

Thermal motion of the lattice was achieved by displacing initial positions of the ions from their ideal (optimized) positions prior to the beginning of the simulation. The amplitude of displacement was chosen randomly for each atom, to a maximum of 0.038 6 a.u. along each Cartesian axis. This displacement was found to yield the desired temperature and MSD (see §3.3.2 regarding temperature).

3.2.4   Electronic structure

Electronic structure calculations were performed using PWscf, a code within the Quantum ESPRESSO package. A basis set cutoff of 50 Ry was used for all parts of the electronic structure calculations. The self-consistent calculations to obtain the potential field were performed on the same 12 **k**-point grid as the MD calculations.

3.2.5   Vibrational analysis

Atomic positions extracted from the MD simulations were differentiated with a simple 3-point scheme to obtain the velocities of each particle. The vibrational density of states

(VDOS) was computed via Fourier transformation of the velocity autocorrelation (VAC) function, defined as

$$Z(t) = \frac{\langle \mathbf{v}(0) \cdot \mathbf{v}(t) \rangle}{\langle \mathbf{v}(0) \cdot \mathbf{v}(0) \rangle}. \tag{3.1}$$

The Fourier transform of the VAC is then $F(\omega) = \int_{-\infty}^{\infty} dt\, e^{i\omega t} Z(t) / \sqrt{2\pi}$, making the vibrational density of states $\Phi(\omega) = F^2(\omega)$.

The relatively short duration of AIMD simulations calls question to the interpretation of the peak heights of the VDOS. If the system has not fully thermalized, then the relative peak heights are best interpreted only as the relative occupation of phonon modes, and the absolute peak heights have little significance. Hence, it is sufficient and favourable to only consider the real (i.e., the cosine) part of the transform:

$$f(\omega) = \frac{1}{\sqrt{2\pi}} \int_0^{\infty} dt\, Z(t) \cos \omega t.$$

The absolute peak heights of f have no physical relevance but to distinguish the frequencies at which dominant phonon modes appear. The peaks in f are however sharper than the corresponding peaks in F^2 making it easier to pinpoint the phonon frequencies. The heights of the peaks in f are not as strictly defined as those if F^2, but they can be loosely interpreted in a similar sense.

Because the velocity data was sampled discretely, the VAC function can be calculated neither exactly nor for an arbitrary length of time. The times at which we can compute the VAC function must be in step with the MD time array. For a simulation with M time steps, the mth element of the VAC, $\hat{Z}_m$, can be computed as [72]

$$\hat{Z}_m = \frac{1}{M-m} \sum_{n=0}^{M-m-1} \frac{\langle \mathbf{v}[t_{n+m}] \cdot \mathbf{v}[t_n] \rangle}{\langle \mathbf{v}[t_0] \cdot \mathbf{v}[t_0] \rangle}. \tag{3.2}$$

The summand in this equation is a direct extension of Eq. (3.1) to a discretely sampled velocity array. The summation is used so that $\hat{Z}_m$ is an average of all possible VAC that can be constructed from the velocity data, by shifting our origin in time by m steps. The problem with moving the origin by m steps is that it becomes m steps closer to the end of the data set (with M elements). This makes the subsequent VAC functions smaller by m elements, and is why each $\hat{Z}_m$ in Eq. (3.2) is scaled by a factor $(M-m)^{-1}$. This makes the estimator statistically unbiased.

The Fourier transform is performed on $\hat{Z}_m$ using the FFTW 3.2.x package [73, 74]. The full Fourier transform, $F(\omega) = F_1(\omega) + iF_2(\omega)$, is computed, but as stated earlier, it is sufficient to analyse only $\mathfrak{R}\{F\} = F_1$. It is useful to normalize the data so that the

56

highest peak has a value of unity, allowing two spectral plots to be compared without large differences in peak heights reducing the readability of the plots.

3.3 Results and Discussion

The results are divided into four parts: relaxation studies, molecular dynamics, electronic structure and vibrational analysis. The relaxation studies (§3.3.1) yield the (unperturbed) starting geometry and **k**-points used in the MD simulation (§3.3.2). The MD simulation yields the configurations for electronic structure calculations (§3.3.3) and trajectories for vibrational analysis (§3.3.4).

3.3.1 Surface relaxation studies

We begin by examining the relaxation studies performed on the surface. We compare our results closely to those of Iarlori *et. al.* (Ref. 51), since that work is the only other study of the dynamics of the $C(111)\,2 \times 1$ surface that we could find. It is important to mention that Iarlori's group found dimerization in the relaxed surface that we believe to be unphysical. In our studies, we endeavour to find an undimerized and unbuckled relaxed surface.

To that end, the 4×2 cell was relaxed on various **k**-point meshes, the results of which are given in Table 3.2 (which is a summary of all relaxation results). We see a trend established between **k**-point mesh density and ideality of the surface. As the **k**-mesh density is increased—making the calculations more accurate—the surface qualitatively approaches the ideal Pandey geometry. Due to the computational expense associated with these relatively large calculations, it was important to find a **k**-mesh which could be used effectively for MD, but mitigate computational requirements.

Two different **k**-mesh generators were used. The simplest generator calculated a uniform mesh across the entire BZ (Figure 3.2) and the second generator used the algorithm of Monkhorst and Pack [75], sampling only the IBZ.

The only mesh which yielded satisfactory levels of buckling and dimerization on the 4×2 cell was the 12 **k**-point uniform mesh. Hence, this mesh was used for MD calculations and electronic structure calculations for the 4×2 cell. We compare with Iarlori, who used the $\bar{\Gamma}$-point only, and a 20 Ry cut-off. Iarlori's group obtained an unbuckled surface with 1.4% dimerization. We attempted the same calculation with $\bar{\Gamma}$-point only, and 20 Ry cut-off, and obtained an unbuckled surface with 3.6% dimerization. This is an indication that Iarlori's carbon PP may have been softer, and therefore better represented by a basis set with a

Table 3.2: Summary of relaxation studies on 2×1, 4×2 and 4×4 systems with various calculation parameters indicated. Unless otherwise noted, all of the present calculations were performed with a basis set cutoff $E_{\mathrm{cut}} = 50$ Ry. Uniform **k**-grid dimensions are specified by '$\times$' symbols and MP [75] grid parameters are separated by commas (,) which can be used to distinguish the two types.

Type	System	**k**-grid	n_{kpt}	$\langle |d| \rangle$ (%)	Δ (Å)	E_{cut}/Notes
CP	2×1	unknown	36	1.4	0.	35 Ry/Ref. 51
BO	2×1	3,6,2	18	0.00	0.006	
BO	4×2	$3 \times 4 \times 1$	12	0.00	0.006	
BO	4×2	3,6,1	10	1.25	0.005	
BO	4×2	$2 \times 3 \times 1$	6	3.06	0.005	
BO	4×2	2,4,1	6	2.39	0.004	
CP	4×2	$\bar{\Gamma}$	1	5.97	0.003	
CP	4×2	$\bar{\Gamma}$	1	1.4	0.	20 Ry/Ref. 51
CP	4×2	$\bar{\Gamma}$	1	3.67	0.003	20 Ry
BO	4×4	$6 \times 6 \times 1$	36	0.00	0.005	

smaller cut-off. Soft-core PPs are known to have transferability issues, which may or may not have affected their results.

We also perform calculations on the 2×1 cell, for the sake of completeness and comparison to Iarlori's results. With relatively little computational effort, we converge to an unbuckled and undimerized surface; confirming once again the notion that well converged DFT should yield an ideal Pandey surface for C(111) 2×1. Iarlori's group, however, still obtained a dimerized surface, despite having a more sophisticated and dense BZ sampling. Note though, that Iarlori's group uses 35 Ry cut-off, whereas we obtain our undimerized surface with a 50 Ry cut-off. It would however be inappropriate for us to lower our cut-off, as we have already seen that our carbon PP requires us to use a larger number of plane-waves.

Larger order reconstructions were investigated with the 4×4 cell, which is larger than any we have seen in published DFT investigations of this surface. No long range patterns were shown, and instead, the surface converged simply as eight unbuckled and undimerized 2×1 cells. This is the final confirmation that the C(111) 2×1 surface relaxes to the ideal Pandey model within well converged DFT calculations.

3.3.2   Molecular dynamics

The molecular dynamics simulation was run for 5 724 time steps, or 4.153 7 ps. The average temperature of the slab was approximately 820 K as calculated by Equation (2.3). Over the
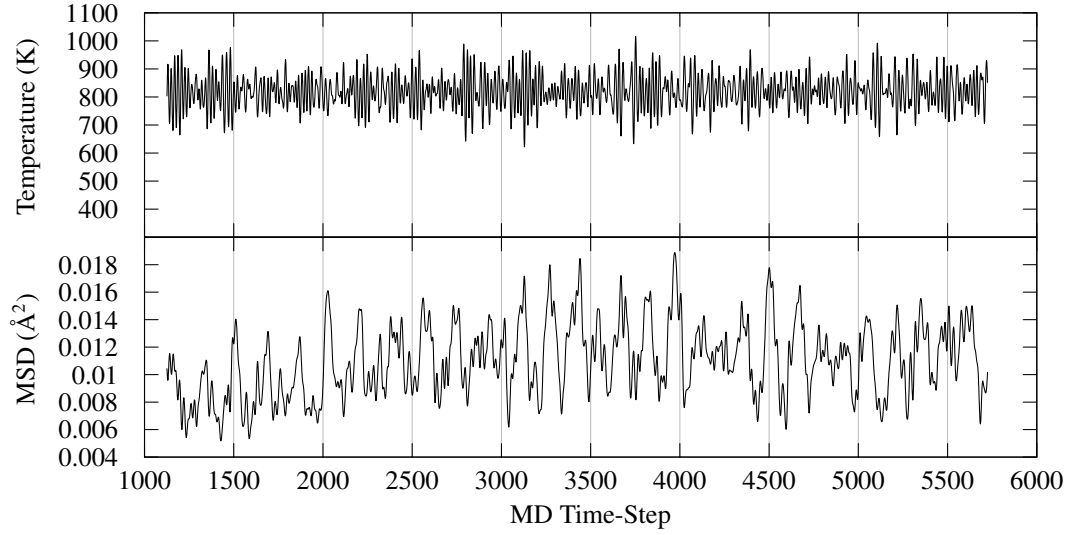
Figure 3.5: MSD and Temperature for the C(111) 2 × 1 MD trajectory. The initial time steps which were not used for data acquisition are not shown.

course of the simulation, there was no significant buckling on average. The absolute average dimerization was roughly 2.4%, while the non-absolute averages were approximately zero. This confirms that the system tended towards an undimerized and unbuckled surface during dynamics. The time evolution of the instantaneous temperature and MSD is shown in Figure 3.5. We believe that the average temperature of 820 K corresponds to an empirical temperature of roughly 300 K, once the contributions from zero-point motion are removed.

The initial randomization of coordinates naturally leads to energy variations from one atom to the next. As the simulation progresses and the phonon modes propagate, these variations are generally smoothed out. The two fixed layers at the centre of the slab however, prevented the exchange of phonons between the top and bottom halves of the slab resulting in the two sides of the slab having two distinct temperatures. Figure 3.6 shows the temperature and MSD of each layer of the slab separately, where it is clear that the top of the slab is on-average hotter than the bottom.

Perhaps more interesting, is the observed temperature difference between the two chains on the top half of the slab. Referring once again to Figure 3.2, we designate the first chain to be the AB chain, and the second to be the CD chain. The average temperature of the first chain is 868 K, while the average temperature of the second chain is 812 K. The spatial separation of the chains restricts the propagation of phonons in the $[11\bar{2}]$ direction at the top layer; so thermalization cannot take place in timescales that are practical for *ab-initio* MD
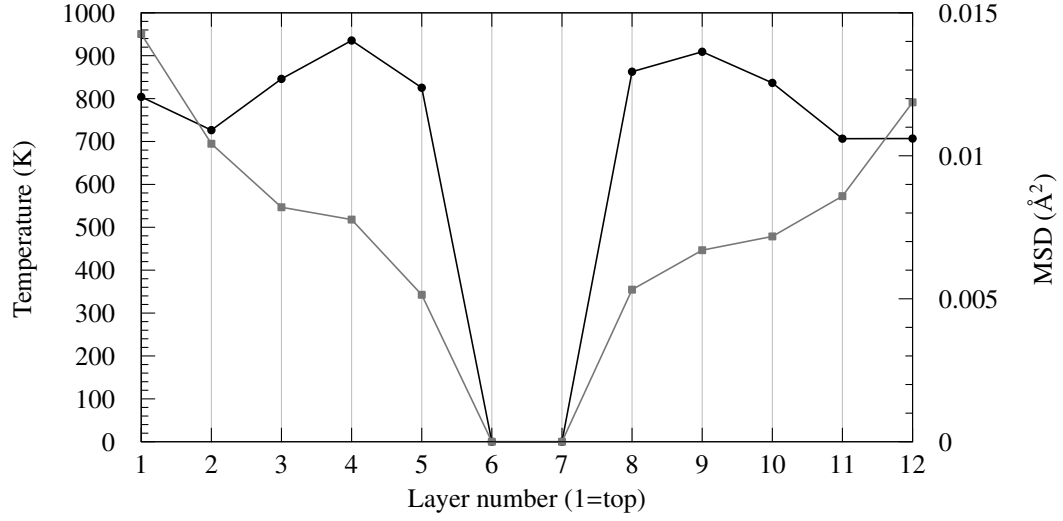
59

Figure 3.6: The time averaged temperature (black lines with circles) and MSD (grey lines with boxes) for each layer of the 4×2 cell over the MD trajectory.

simulations. As a result, the occupation of phonon modes is very different between the two chains.

We will see these temperature differences manifested later, in the analysis of the slab's electronic structure. However, it should not significantly affect the vibrational properties of the system. At temperatures for which the potential is approximately harmonic, thermal vibrations affect the population of phonon modes, but not the frequencies.

3.3.3 Electronic structure

One of the main goals of the research is to determine if the natural vibrations of the $C(111) 2 \times 1$ surface observe modes which open the electronic gap between the surface π and π^* states. A thorough analysis of the surface harmonics is to come. However, without much effort, one can ascertain a great deal about the system's harmonics directly from the fluctuations in MSD and temperature. The high frequency range of phonon modes is expressed in fluctuations of temperature, which is a quantity sensitive to microscopic changes in energy. The lower frequency of range phonon modes is more easily distinguished in the MSD, which is less sensitive to microscopic changes and tends to capture the essence of the motion of the entire slab.

From Figure 3.5, we can roughly estimate one of the lower frequency modes of the system around the series of peaks which occur in intervals of approximately 160 time-steps,

Table 3.3: Surface statistics and gap analysis [76] for 10 instantaneous configurations sampled at constant intervals during a long period oscillation of the MD trajectories. Negative values for E_g indicate a semi-metallic overlap of π and π^*.

Sample	Time-Step	Δ (Å)	$\langle |d| \rangle$ (%)	Energy Gaps (eV)		
				$\bar{\Gamma}$	$\bar{J}'$	E_g
1	5130	0.06	1.75	0.11	0.04	0.05
2	5148	0.07	1.93	0.15	0.15	0.15
3	5166	0.05	1.77	0.15	0.13	0.11
4	5184	0.08	1.93	0.23	0.02	0.05
5	5202	0.03	1.90	0.17	0.03	0.08
6	5220	0.08	2.30	0.01	0.12	0.05
7	5238	0.03	3.53	0.02	0.31	0.14
8	5256	0.08	2.73	0.02	0.11	−0.02
9	5274	0.03	2.87	0.13	0.09	0.02
10	5292	0.05	0.84	0.05	0.1	−0.06

or $0.117\,5$ ps. We arbitrarily pick one of these intervals and sample it at ten evenly timed sub-intervals. According to the sampling theory, this captures the harmonics of the system less than 42.553 THz or $1\,419.4\,\text{cm}^{-1}$, which we will see later, is adequate to represent the essential vibrations of the entire slab. The electronic structure is calculated at each of these samples, and the gap between π and π^* states at $\bar{\Gamma}$ and $\bar{J}'$ are measured, as well as the indirect gap[1] between $\bar{\Gamma}$ and $\bar{J}'$. These calculations are summarized in Table 3.3. In that table, we see the first confirmation that the natural vibrations of the surface open the gap. Of the ten samples, only two of them show any signs of semi-metallic character; and as we shall soon demonstrate, the origin of the overlap may be localized to only one of the four chains of the slab.

To gain a more intuitive understanding of the effects of electron-phonon interaction, it is useful to directly compare the electron band-structure for ideal and thermally perturbed structures. In Figure 3.7 electron bands are plotted for both the ideal lattice and the configuration corresponding to sample 2 of Table 3.3, along high symmetry lines of the BZ. The surface bands below the Fermi level are the π states, with the highest energy π state (i.e., the HOMO) found at $\bar{\Gamma}$. The surface bands above the Fermi level are the π^* states, with the lowest energy π^* state (i.e., the LUMO) at $\bar{J}'$. For the ideal case, there is no discernible gap between the π and π^* states. But in the thermally perturbed case, we see a gap of 0.15 eV.
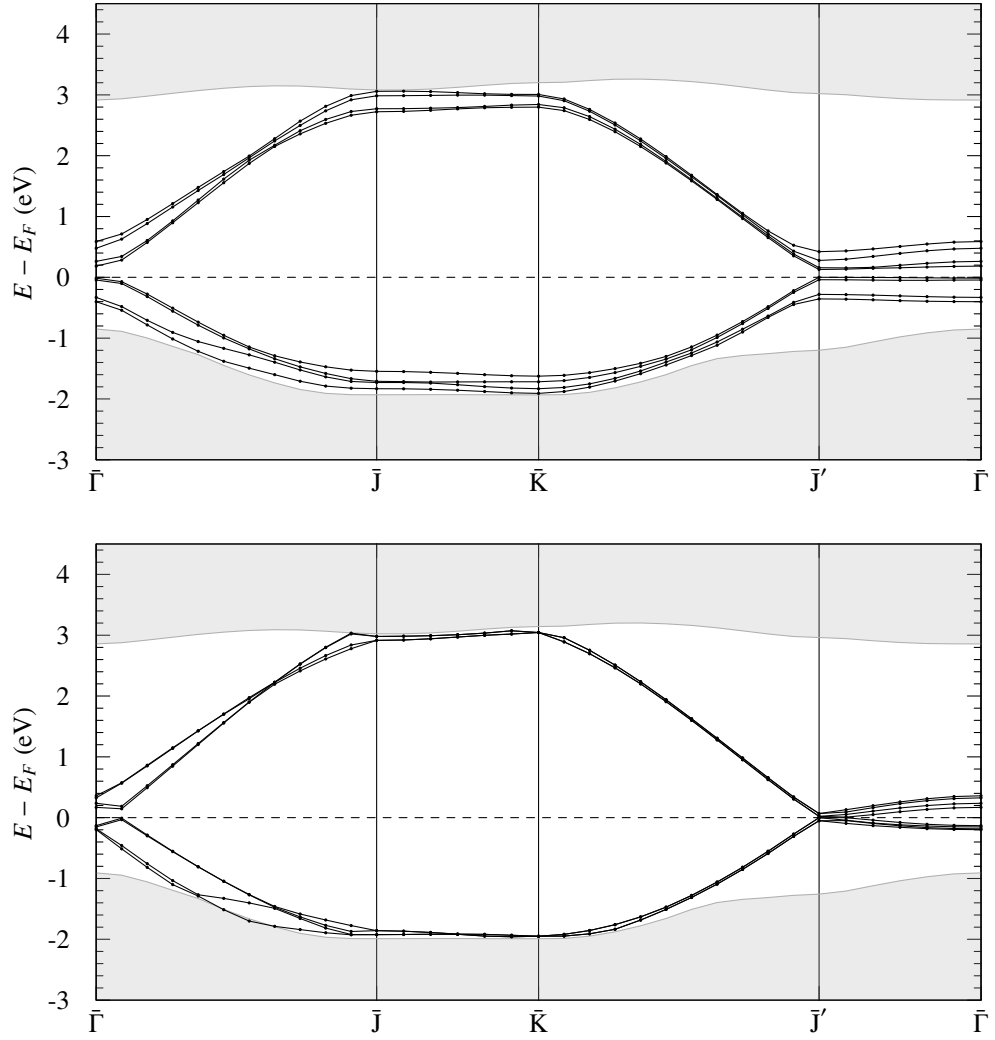
---

[1]Which is the true band-gap.

Figure 3.7: Electron band plots comparing the structure of the thermally perturbed lattice (top panel) and the ideal lattice (bottom panel). Projected bulk states are shaded in grey and the surface bands are shown with black lines and circles. The Fermi level is set at zero and represents the energy of the HOMO. The band-gap, E_g, can be identified as the difference in energy between the HOMO at $\bar{\Gamma}$ and the LUMO, which is found at $\bar{J}'$.

For the 4×2 cell, there are four π bands with four corresponding π^* bands. Each band comes from a different chain with two chains on each of the top and bottom surfaces of the slab.

Without further investigation, it is impossible to know which bands correspond to which chains. To reduce the number of bands near the $\bar{J}'\bar{\Gamma}$ gap, the bottom six layers of both the ideal and thermally perturbed slabs were removed, and the resultant dangling bonds were passivated with atomic hydrogen. The ideal bonding configuration of the hydrogen monolayer with the truncated surface was calculated by geometry relaxation. This procedure removes the contribution of the bottom surface from the region of energy close to the $\bar{J}'\bar{\Gamma}$ gap, allowing us to see only the bands for the top surface chains. The resultant electronic structure, shown in Figure 3.8, demonstrates the described effect. We see essential modification of the bulk states due to the truncation. We also see that the hydrogen bound states of the bottom surface exist within the bulk gap, but are no longer near the energy of the π-bound states on the $\bar{J}'\bar{\Gamma}$ path of the BZ. Most importantly, we see the energy gap is opened slightly more than when both top and bottom surfaces contributed to the electronic structure. Surprisingly though, we do find that the surface bands from the two top chains are very different. This, we believe to be the manifestation of the difference in temperatures (and phonon populations) between the two chains, which was discussed in §3.3.2.

3.3.4   Vibrational analysis

No experimental data exists for the vibrations of the surface layers of C(111) 2×1. So we first perform an analysis on diamond bulk, for which the VDOS has been studied experimentally and theoretically [77, and references therein]. A straightforward MD simulation for a 64-atom cubic cell of bulk diamond was run using the same cut-off and time step as for the 4×2 slab. The cubic BZ was sampled at the Γ-point, and the duration of the simulation was $10\,000$ time-steps. The vibrational spectrum calculated from these data are compared with experimentally measured VDOS in Figure 3.9. Some Gaussian broadening has been applied to the theoretical line in that figure because the limited sampling of momentum space (at the $\bar{\Gamma}$ point only) limits the number of vibrational modes of the atoms. We analyse the positions of the peaks in the theoretical data, and gauge their alignment to the main features of the experimental data. The agreement shown in Figure 3.9 is excellent, and is a very good indication that our procedure is sound.

Continuing now to the 4×2 slab, it is useful to decompose the vibrational spectrum. We calculated the spectra of the whole slab, and the top layer only. Then, the vibrations of the top layer were further broken down into vibrations along the chains in the $[\bar{1}10]$
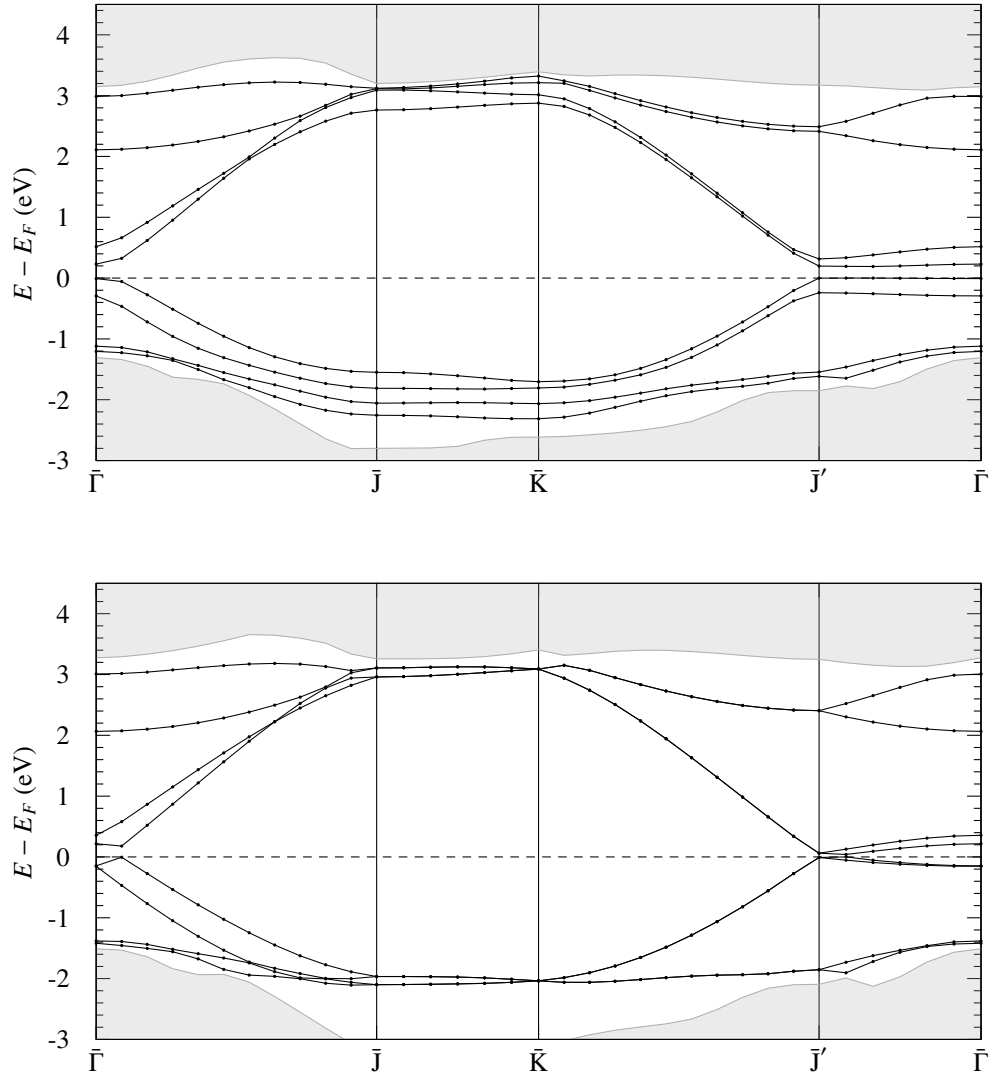
Figure 3.8: The panels in this figure correspond to those in Figure 3.7. Here, the contributions of the bottom of the slab have been removed by truncation and hydrogen termination. The hydrogen states are seen between the surface states and the projected bulk states.
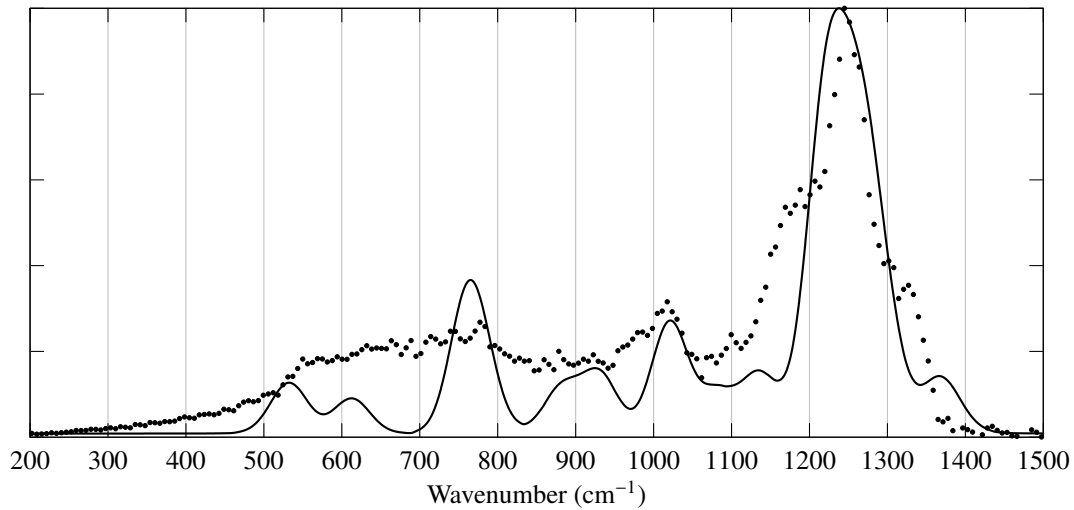
Figure 3.9: The real part of the Fourier transform of the VAC for MD of a cubic 64-atom diamond bulk cell (black line) with the experimentally measured VDOS of diamond bulk from Ref. 77.

direction, perpendicular to the chains in the $[11\bar{2}]$ direction and perpendicular to the surface in the $[111]$ direction. These spectra are plotted in Figure 3.10. This figure allows us to identify which vibrational peaks belong to specific modes of vibration. To begin, the top panel distinguishes which modes are unique to the bulk, which are shared between the bulk and surface and which are unique to the surface.

The two largest peaks of the 'Whole Slab' spectrum appear to originate from the optical phonon modes of the bulk. They are lower in frequency than the corresponding peaks in Figure 3.9, but this is expected because the surface to volume ratio of the slab is very high in comparison to an experimental sample. In nature, the effects of the surface are felt many layers down into the bulk; so a 12-layer slab does not contain any bulk layers that are truly isolated from the effects of the surface. Because the surface weakens the sub-structure, the bonds are softened and frequencies are lowered.

Moving now to the analysis of the directional decomposition of the spectrum, we consider which data are relevant to our outcome. Vibrations in the $[111]$ direction are expected to mostly associate with buckling modes, or the vibration of the entire top layer with respect to the second layer. However, if there is a twisting mode, in which the dimers rotate slightly, we will see this expressed in the $[111]$ direction. The π bonds of the surface chains have components in the $[11\bar{2}]$ and $[\bar{1}10]$ direction, so harmonic distortions of the bond lengths (dimerization modes) are expected to be expressed in these directions.

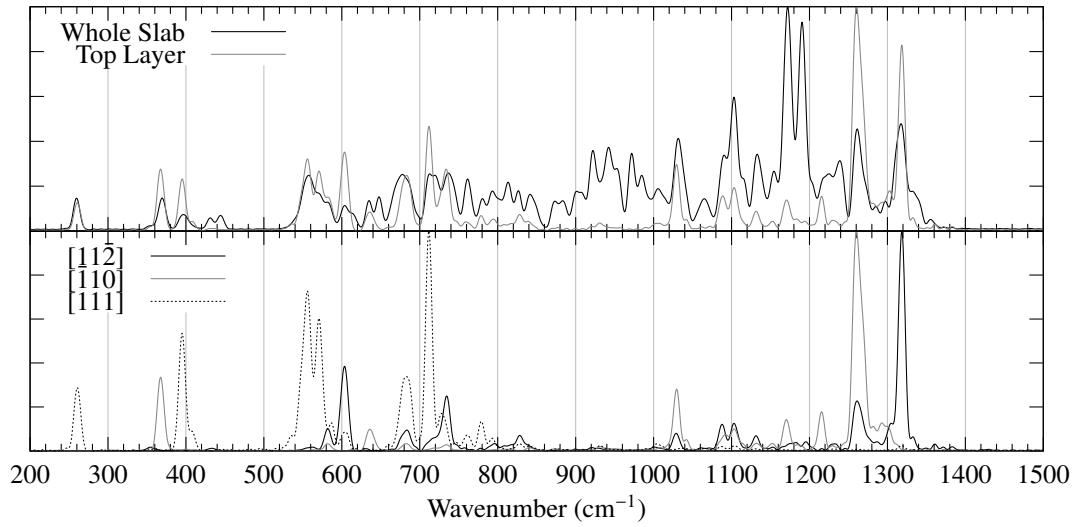Since dimerization modes are the ones which have been shown to open the gap, we

Figure 3.10: The real parts of the VAC Fourier transform for dynamics of the 4×2 slab. In the top panel, vibrational data for the whole slab and the top surface layer are plotted. In the bottom panel, vibrations of the top layer are decomposed along the $[11\bar{2}]$, $[\bar{1}10]$ and $[111]$ directions.

focus on identifying these corresponding peaks in the spectra. To do this, we calculate the dimerization coefficient, $d_0[t]$, for an arbitrary dimer at each time-step t of the MD run. The discrete Fourier transform of $d_0[t]$ is calculated, and plotted against the surface vibrational data in Figure 3.11. We see here that 10 distinct peaks are immediately identifiable in the spectrum of d_0. The strongest peak in d_0, at approximately $1\,262\,\text{cm}^{-1}$ corresponds exactly to the main peak of the entire top layer, which is seen to come from the $[\bar{1}10]$ direction. A complete break-down of which peaks of the spectrum of d_0 are expressed in which direction is found in Table 3.4.

One peak of the d_0 spectrum, with a frequency of $1\,117\,\text{cm}^{-1}$ appears to have no associated direction. These vibrations are expressed along the $[11\bar{2}]$ direction, where there are vibrations but no corresponding peak. This peak is an artefact of the particular dimer chosen for d_0, and is lost when the vibrations of the whole top layer are considered.

3.4   Conclusion

The C(111) 2×1 surface has been a source of conflict between experiment and theory for more than two decades. The source of this conflict is associated not only with DFT calculations of electronic structure, but also with the geometry of the lattice used for
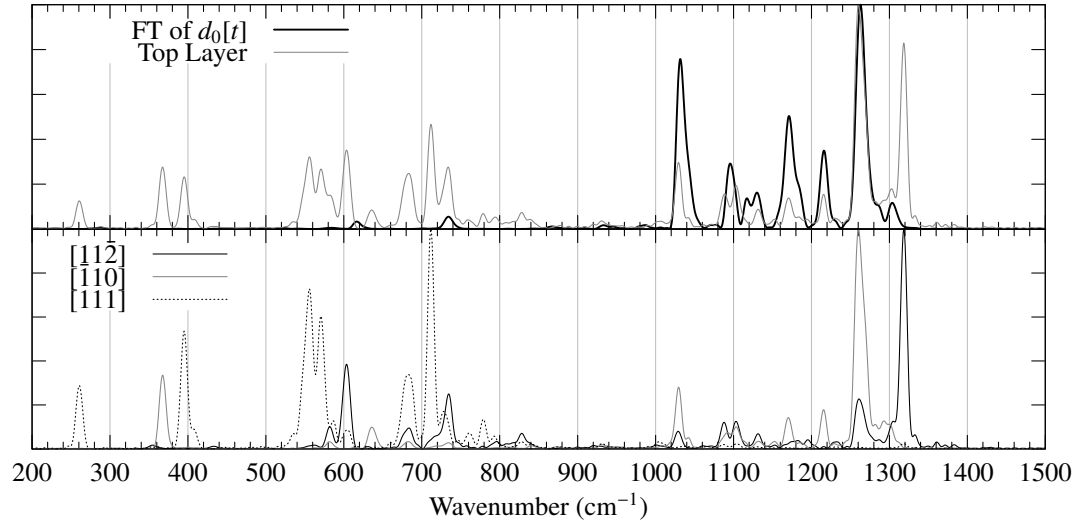
Figure 3.11: The Fourier transform of one of the dimerization coefficients is plotted in the top panel along with the vibrational data for the top layer. In the bottom panel, vibrations of the top layer are decomposed along the $[11\bar{2}]$, $[\bar{1}10]$ and $[111]$ directions, for comparison to the above Fourier transform on the dimerization coefficient.

Table 3.4: A tabular decomposition of dimer frequencies along crystal axes. A '1' indicates that the dimer frequency is expressed in the direction corresponding to that column, and a '-' indicates that it is not.

Frequency (cm^{-1})	$[11\bar{2}]$	$[\bar{1}10]$	$[111]$
1 303	1	1	-
1 262	-	1	-
1 216	-	1	-
1 182	-	1	-
1 130	1	1	-
1 117	-	-	-
1 095	1	1	-
1 031	1	1	-
734	1	-	-
617	1	-	1

calculation. Attempts to extend the DFT results under the *GW* approximation have failed due to the use of metallic DFT wave-functions. We have proposed and shown that once the effect of electron–phonon interaction under naturally perturbed lattice geometries is considered, the gap is opened and DFT wave-functions can be extended within the *GW* framework.

More generally, we have demonstrated that the natural vibrations of the surface effectively open the gap between surface π and π^* states. These vibrations, even at room temperature will be intense due to the exceptionally high zero-point lattice energy of diamond. Furthermore, we have investigated the vibrational spectrum of the surface and identified the primary frequencies of modes associated with dimerization: the mechanism shown to be effective at opening the surface gap.

Conclusion and Future Outlook

WE have proposed a general numerical formalism which—for the first time—explicitly accounts for the effects of electron–phonon interaction in the electronic structure of semiconductors and those properties which depend on band–structure modification. These effects are crucial to capturing the essential physics seen in experiments. Results have been presented for the method applied to two problems: (1) the calculation of the temperature dependent linear optical dielectric function of GaAs and (2) modelling the electronic structure modification of the $C(111)\,2 \times 1$ surface due to surface vibrations. These problems have each been shown to be relevant on their own and both give insight into the validity of the theoretical approach.

The temperature dependent linear optical response of GaAs was an excellent proving ground for our method because it directly summarizes the effects of electron–phonon interaction in a way that can be qualitatively and quantitatively observed. The qualitative effects of temperature on the linear dielectric function, seen from experiment were also present in our modelled data. The quantitative analysis was also favourable, showing a reproduction of the experimentally observed temperature dependent trends, to well within the expected accuracy of the theoretical methodology. This is the first time that such effects have been modeled within a first principles approach.

The electronic structure of the $C(111)\,2 \times 1$ surface, a source of mystery in modern science, was studied from the perspective of surface vibrational properties and modification of the electronic structure. Materials related to this surface are becoming quite fashionable in the world of materials science due to their exceptional properties. This was the first study (with this depth) to be performed on the surface, due to the computational formidability. We have shown that the generally accepted model for the geometry of the surface cannot naturally exist in its ideal form. As a minimal example of this, key modes of vibration were linked to specific distortions of the surface which bring electronic structure calculations

closer to agreement with experiment. More than this, we have provided a method for obtaining wave-functions for the surface which can be used appropriately as the zeroth-order approximation to be extended by more advanced electronic structure calculations such as the self-consistent *GW* method.

The individual treatment of these problems adds incrementally to the span of scientific knowledge. But the value of the method described in these pages is key for future development in this field. There is no doubt that more sophisticated methods will be developed in the future, as computers become more capable. But this method represents the first step toward inclusion of electron–phonon interaction in standard DFT models. This will allow scientists to define temperature dependent properties and model experimental results in a more complete way and gives DFT true predictive power in non-ground-state lattices.

In future outlook, the method may be applied to many more systems and calculation types. The calculation of temperature dependant optical properties, as in Chapter 2, could be immediately extended to other materials. Despite this document's focus on GaAs, the method has already been successfully applied to the system of crystalline silicon bulk [32]. Any further refinement involves simply adjusting algorithms and parameters within the individual DFT and MD calculations to suit the particular material system and computing environment chosen by the researcher.

With respect to the $C(111)\, 2 \times 1$ problem presented in Chapter 3, research is continued in order to fully explain the experimentally observable semiconducting properties of the surface. Currently, the presence of hydrogen contamination and it's impact on the surface gap and geometry is being investigated in a manner similar to the studies described in Chapter 3.

[1] E. Schrödinger. An Undulatory Theory of the Mechanics of Atoms and Molecules. *Phys. Rev.*, 28(6):1049–1070, Dec 1926.

[2] J. C. Slater. The Self Consistent Field and the Structure of Atoms. *Phys. Rev.*, 32(3):339–348, Sep 1928.

[3] J. C. Slater. The Theory of Complex Spectra. *Phys. Rev.*, 34(10):1293–1322, Nov 1929.

[4] J. C. Slater. A Simplification of the Hartree-Fock Method. *Phys. Rev.*, 81(3):385–390, Feb 1951.

[5] V. Fock. Näherungsmethode zur Lösung des quantenmechanischen Mehrkörper-problems. *Zeitschrift für Physik A Hadrons and Nuclei*, 61(1):126–148, 01 1930. 10.1007/BF01340294.

[6] P. Hohenberg and W. Kohn. Inhomogeneous Electron Gas. *Phys. Rev.*, 136(3B):–864, Nov 1964.

[7] W. Kohn and L. J. Sham. Self-Consistent Equations Including Exchange and Correlation Effects. *Phys. Rev.*, 140(4A):–1133, Nov 1965.

[8] M. C. Payne, M. P. Teter, D. C. Allan, T. A. Arias, and J. D. Joannopoulos. Iterative minimization techniques for ab initio total-energy calculations: molecular dynamics and conjugate gradients. *Rev. Mod. Phys.*, 64(4):1045–1097, Oct 1992.

[9] B.H. Bransden and C.J. Joachain. *Physics of Atoms and Molecules*. Pearson Education Limited, Essex, England, 2nd edition, 2003.

[10] David Griffiths. *Introduction to Quantum Mechanics*. Prentice Hall, Upper Saddle River, NJ, 2nd edition, 2005.

[11] Frank L. Pilar. *Elementary Quantum Chemistry*. McGraw-Hill Pub., New York, 2nd edition, 1990.

[12] Matthias Ernzerhof, John Perdew, and Kieron Burke. *Density Functional Theory I: Functionals and Effective Potentials*, volume 180 of *Topics in Current Chemistry*, chapter Density functionals: Where do they come from, why do they work?, pages 1–30. Springer, Berlin/Heidelberg, 1996.

[13] Paolo Giannozzi. Lecture Notes per il Corso di Struttura della materia: Density Functional Theory for Electronic Structure Calculations. Available at http://www.democritos.it/events/pw-tutorial/lectures/dft_theory.pdf, 2005.

[14] J. P. Perdew and Alex Zunger. Self-interaction correction to density-functional approximations for many-electron systems. *Phys. Rev. B*, 23(10):5048–5079, May 1981.

[15] Paula Mori-Sánchez, Aron J. Cohen, and Weitao Yang. Localization and Delocalization Errors in Density Functional Theory and Implications for Band-Gap Prediction. *Physical Review Letters*, 100(14):146401, 2008.

[16] Aron J. Cohen, Paula Mori-Sanchez, and Weitao Yang. Insights into Current Limitations of Density Functional Theory. *Science*, 321(5890):792–794, 2008.

[17] Aron J. Cohen, Paula Mori-Sanchez, and Weitao Yang. Fractional spins and static correlation error in density functional theory, 2008.

[18] Aron J. Cohen, Paula Mori-Sánchez, and Weitao Yang. Fractional charge perspective on the band gap in density-functional theory. *Physical Review B (Condensed Matter and Materials Physics)*, 77(11):115123, 2008.

[19] Paula Mori-Sánchez, Aron J. Cohen, and Weitao Yang. Discontinuous Nature of the Exchange-Correlation Functional in Strongly Correlated Systems. *Physical Review Letters*, 102(6):066403, 2009.

[20] John P. Perdew, Kieron Burke, and Matthias Ernzerhof. Generalized Gradient Approximation Made Simple. *Phys. Rev. Lett.*, 77(18):3865–3868, Oct 1996.

[21] Charles Kittel. *Introduction to Solid State Physics*. John Wiley and sons, New-York, 8th edition, 2005.

[22] E. Sjöstedt, L. Nordström, and D. J. Singh. An alternative way of linearizing the augmented plane-wave method. *Solid State Communications*, 114(1):15–20, 2000.

[23] J. C. Slater. Wave Functions in a Periodic Potential. *Phys. Rev.*, 51(10):846–851, May 1937.

[24] David Singh. Ground-state properties of lanthanum: Treatment of extended-core states. *Phys. Rev. B*, 43(8):6388–6392, Mar 1991.

[25] Peter Balah, Karlheinz Schwars, Georg Madsen, Dieter Kvasnicka, and Joachim Luitz. *WIEN2k: An Augmented Plane Wave Plus Local Orbitals Program for Calculating Crystal Properties*. Vienna, Austria, April 2008.

[26] D. Marx and J. Hutter. Ab initio molecular dynamics: Theory and implementation; Modern Methods and Algorithms of Quantum Chemistry. *NIC Series*, 31:195–244, 2006.

[27] R. Car and M. Parrinello. Unified Approach for Molecular Dynamics and Density-Functional Theory. *Phys. Rev. Lett.*, 55(22):2471–2474, Nov 1985.

[28] M. A. Herman, W. Richter, and H. Sitter. *Epitaxy: Physical Principles and Technical Implementation*, volume 62 of *Springer Series in Materials Science*. Springer Verlag, New York, 2004.

[29] Lars Hedin. New Method for Calculating the One-Particle Green's Function with Application to the Electron-Gas Problem. *Phys. Rev.*, 139(3A):–796, Aug 1965.

[30] F. Aryasetiawan and O. Gunnarsson. The GW method. *Reports on Progress in Physics*, 61(3):237–312, 1998.

[31] Christoph Friedrich and Arno Schindlmayr. Many-Body Perturbation Theory: The GW Approximation. *NIC Series*, 31:335–355, 2006.

[32] Z. A. Ibrahim, A. I. Shkrebtii, M. J. G. Lee, K. Vynck, T. Teatro, W. Richter, T. Trepk, and T. Zettler. Temperature dependence of the optical response: Application to bulk GaAs using first-principles molecular dynamics simulations. *Physical Review B (Condensed Matter and Materials Physics)*, 77(12):125218, 2008.

[33] Peter Y. Yu and Manuel Cardona. *Fundamentals of Semiconductors*. Physics and Materials Properties. Springer Berlin Heidelberg, Berlin, 3 edition, 2001.

[34] J. I. Gersten and F. W. Smith. *The Physics and Chemistry of Materials*. John Wiley & Sons, New York, 2001.

[35] Thomas Trepk. *The Dielectric Funtion of III-V Semiconductors at High Temperatures*. PhD thesis, Technischen Universit at Berlin, Berlin, Germany, 2005.

[36] Sadao Adachi. *GaAs and Related Materials: Bulk Semiconducting and Superlattice Properties*. World Scientific Publishing Co. Pte. Ltd., Singapore, 1994.

[37] Ashley H. Carter. *Classical and Statistical Thermodynamics*. Prentice Hall, Upper Saddle River, NJ, 2001.

[38] Paolo Giannozzi, Stefano de Gironcoli, Pasquale Pavone, and Stefano Baroni. Ab initio calculation of phonon dispersions in semiconductors. *Phys. Rev. B*, 43(9):7231–7242, Mar 1991.

[39] O. Madelung, U. Rössler, and M. Schulz, editors. *Numerical Data and Functional Relationships in Science and Technology*. Landolt-Börnstein, New Series, Group IIIm Vol. 41, Pt. A1a. Springer-Verlag, Berlin, 2001. 10.1007/10551045_108.

[40] S. S. Gorelik V. T. Bublik. Über die röntgenographische Analyse der mittleren quadratischen Atomverschiebungen in einigen Halbleiterkristallen. *Kristall und Technik*, 12(8):859–869, 1977.

[41] D. Olguín, M. Cardona, and A. Cantarero. Electron-phonon effects on the direct band gap in semiconductors: LCAO calculations. *Solid State Communications*, 122(11):575–589, 2002.

[42] S. Baroni, A. Dal Corso, S. de Gironcoli, P. Giannozzi, C. Cavazzoni, G. Ballabio, S. Scandolo, G. Chiarotti, P. Focher, A. Pasquarello, K. Laasonen, A. Trave, R. Car, N. Marzari, and A. Kokalj. Quantum–ESPRESSO package provided by www.quantum-espresso.org.

[43] X. Gonze. Information for Ga pseudopotential available at `http://www.quantum-espresso.org/pseudo/1.3/UPF/Ga.pz-bhs.UPF`.

[44] Xavier Gonze, Roland Stumpf, and Matthias Scheffler. Analysis of separable potentials. *Phys. Rev. B*, 44(16):8503–8513, Oct 1991.

[45] P. Blaha, K. Schwarz, G. Madsen, D. Kvasnicka, and J. Luitz. `http://www.wien2k.at/`.

[46] R. Del Sole and Raffaello Girlanda. Optical properties of semiconductors within the independent-quasiparticle approximation. *Phys. Rev. B*, 48(16):11789–11795, Oct 1993.

[47] P. Lautenschlager, M. Garriga, S. Logothetidis, and M. Cardona. Interband critical points of GaAs and their temperature dependence. *Phys. Rev. B*, 35(17):9174–9189, Jun 1987.

[48] S. H. Ahn, J. G. Kim, S. J. Park, and K. R. Lee. Electrochemical behavior of diamond-like carbon films for biomedical applications. *Thin Solid Films*, 475(1-2):291–297, 2005.

[49] F. Bechstedt, W. G. Schmidt, and A. Scholze. Dimerized, buckled, or ideal chains on the diamond $(111)2 \times 1$ surface? *Surface Science*, 351(1-3):183–188, 05 1996.

[50] M. Marsili, O. Pulci, F. Bechstedt, and R. Del Sole. Electronic structure of the C(111) surface: Solution by self-consistent many-body calculations. *Phys. Rev. B*, 72(11):115415, Sep 2005.

[51] Simonetta Iarlori, Giulia Galli, François Gygi, Michele Parrinello, and Erio Tosatti. Reconstruction of the diamond (111) surface. *Phys. Rev. Lett.*, 69(20):2947–2950, Nov 1992.

[52] A. Scholze, W. G. Schmidt, and F. Bechstedt. Structure of the diamond (111) surface: Single-dangling-bond versus triple-dangling-bond face. *Phys. Rev. B*, 53(20):13725–13733, May 1996.

[53] A. A. Stekolnikov, J. Furthmüller, and F. Bechstedt. Absolute surface energies of group-IV semiconductors: Dependence on orientation and reconstruction. *Phys. Rev. B*, 65(11):115318, Feb 2002.

[54] K. C. Pandey. Reconstruction of Semiconductor Surfaces: Buckling, Ionicity, and π-Bonded Chains. *Phys. Rev. Lett.*, 49(3):223–226, Jul 1982.

[55] K. C. Pandey. New π-Bonded Chain Model for Si(111)-(2×1) Surface. *Phys. Rev. Lett.*, 47(26):1913–1917, Dec 1981.

[56] G. Bussetti, C. Goletti, P. Chiaradia, and T. Derry. Optical gap between dangling-bond states of a single-domain diamond C(111)-2×1 by reflectance anisotropy spectroscopy. *EPL (Europhysics Letters)*, 79(5):57002–5, 2007.

[57] Friedhelm Bechstedt. *Principles of Surface Physics*. Springer-Verlag, Berlin, 2003.

[58] Margherita Marsili, Olivia Pulci, Friedhelm Bechstedt, and Rodolfo Del Sole. Tight-binding calculations of quasiparticle wave functions for C(111)2 x 1. *Physical Review B (Condensed Matter and Materials Physics)*, 78(20):205414, 2008.

[59] C. Kress, M. Fiedler, and F. Bechstedt. Quasi-Particle Bands for C(111) 2×1 Surfaces–Support for the Dimerized π-Bonded Chain Model. *EPL (Europhysics Letters)*, 28(6):433–438, 1994.

[60] A. I. Shkrebtii, R. Di Felice, C. M. Bertoni, and R. Del Sole. Ab initio study of structure and dynamics of the Si(100) surface. *Phys. Rev. B*, 51(16):11201–11204, Apr 1995.

[61] David Vanderbilt and Steven G. Louie. Total energy minimization for diamond (111) surfaces: Support for an undimerized π-bonded chain reconstruction. *Phys. Rev. B*, 29(12):7099–7101, Jun 1984.

[62] H. A. Jahn and E. Teller. Stability of Polyatomic Molecules in Degenerate Electronic States. I. Orbital Degeneracy. *Proceedings of the Royal Society of London. Series A - Mathematical and Physical Sciences*, 161(905):220–235, 1937.

[63] Mark A. Prelas, Galina Popovici, and Louis K. Bigelow, editors. *Handbook of Industrial Diamonds and Diamond Films*. CRC Press, New York, New York, 1st edition.

[64] M. H. Grimsditch and A. K. Ramdas. Brillouin scattering in diamond. *Phys. Rev. B*, 11(8):3139–3148, Apr 1975.

[65] J. x. Sun and R. g. Tian. Analytic equation of state and thermodynamic properties of diamond based on an analytic mean field approach. *Diamond & Related Materials*, 18(4):632–636, 04 2009.

[66] P. Giannozzi. Information for C pseudopotential available: http://www.quantum-espresso.org/pseudo/upfdetails.php?upf=C.pz-vbc.UPF.

[67] P. Giannozzi. Information for H pseudopotential available: http://www.quantum-espresso.org/pseudo/1.3/UPF/H.pz-vbc.UPF.

[68] Donald Goldfarb. Variable metric and conjugate direction methods in unconstrained optimization: recent developments. In *ACM'72: Proceedings of the ACM annual conference*, pages 496–506, New York, NY, USA, 1972. ACM.

[69] D. F. Shanno. Conditioning of Quasi-Newton Methods for Function Minimization. *Mathematics of Computation*, 24(111):647–656, July 1970.

[70] R. Fletcher. A new approach to variable metric algorithms. *The Computer Journal*, 13(3):317–322, 1970.

[71] C. G. Broyden. The Convergence of a Class of Double-rank Minimization Algorithms 1. General Considerations. *IMA J Appl Math*, 6(1):76–90, 1970.

[72] Jorge Kohanoff. Phonon spectra from short non-thermally equilibrated molecular dynamics simulations. *Comp. Mat. Sci.*, 2:221–232, 1994.

[73] Matteo Frigo and Steven G. Johnson. The Fastest Fourier Transform in the West. Technical Report MIT-LCS-TR-728, September 1997.

[74] Matteo Frigo and Steven G. Johnson. The Design and Implementation of FFTW3. *Proceedings of the IEEE*, 93(2):216–231, 2005. special issue on "Program Generation, Optimization, and Platform Adaptation".

[75] Hendrik J. Monkhorst and James D. Pack. Special points for Brillouin-zone integrations. *Phys. Rev. B*, 13(12):5188–5192, Jun 1976.

[76] Calculated by our collaborators at University of Rome Tor Vergata.

[77] Alexey Bosak and Michael Krisch. Phonon density of states probed by inelastic x-ray scattering. *Phys. Rev. B*, 72(22):224305, Dec 2005.

INDEX